UNIVERSIDADE FEDERAL DE PERNAMBUCO
CENTRO DE CIÊNCIAS EXATAS E DA NATUREZA
PROGRAMA DE PÓS-GRADUAÇÃO EM FÍSICA

Gabrielle Vaz Accioly

Light structured by thermodynamic principles: Generation of partially-coherent beams from a few to multiple modes

Recife

2025

Gabrielle Vaz Accioly

Light structured by thermodynamic principles: Generation of partially-coherent beams from a few to multiple modes

Dissertação apresentada ao Programa de Pós-Graduação em Física do Departamento de Física da Universidade Federal de Pernambuco como parte dos requisitos para obtenção do título de Mestre em Física

Área de Concentração: Óptica

Orientador: Anderson Monteiro Amaral

Coorientador: Marcio Heraclyto Gonçalves de Miranda

Recife

2025

.Catalogação de Publicação na Fonte. UFPE - Biblioteca Central

Vaz, Gabrielle.
   Light structured by thermodynamic principles: generation of partially-coherent beams from a few to multiple modes / Gabrielle Vaz Accioly. - Recife, 2025.
   65f.: il.

   Dissertação (Mestrado) - Universidade Federal de Pernambuco, Centro de Ciências Exatas e da Natureza, Pós-Graduação em Física, 2025.
   Orientação: Anderson Monteiro Amaral.
   Coorientação: Marcio Heraclyto Gonçalves de Miranda.
   Inclui referências.

   1. Luz estruturada; 2. Óptica termodinâmica; 3. Luz parcialmente coerente. I. Amaral, Anderson Monteiro. II. Miranda, Marcio Heraclyto Gonçalves de. III. Título.

UFPE-Biblioteca Central

GABRIELLE VAZ ACCIOLY

LIGHT STRUCTURED BY THERMODYNAMIC PRINCIPLES: GENERATION OF PARTIALLY-COHERENT BEAMS FROM A FEW TO MULTIPLE MODES

Dissertação apresentada ao Programa de Pós-Graduação em Física da Universidade Federal de Pernambuco, como requisito parcial para a obtenção do título de Mestra em Física.

Área de Concentração: Óptica

Data de aprovação: 06/02/2025.

BANCA EXAMINADORA

_____

Prof. Dr. Anderson Monteiro Amaral
Orientador
Universidade Federal de Pernambuco

_____

Profa. Dra. Sandra Sampaio Vianna
Examinadora Interna
Universidade Federal de Pernambuco

_____

Prof. Dr. Lino Misoguti
Examinador Externo
Universidade de São Paulo

ACKNOWLEDGEMENTS

I acknowledge CNPq (Conselho Nacional de Desenvolvimento Científico e Tecnológico), CAPES (Fundação Coordenação de Aperfeiçoamento de Pessoal de Nível Superior) and FACEPE (Fundação de Amparo à Ciência e Tecnologia de Pernambuco) for the support provided during the development of this work.

ABSTRACT

The coherence state of light is important in several optical systems. This state is also subject to variations due to propagation and imperfections present along the propagation path. Even though changes in the coherence state are common, direct measurements are sometimes difficult and the interpretation complicated, particularly for beams containing few modes. Here, partially coherent beams are analyzed using thermodynamic principles. As far as we know, our approach is novel in the literature and the associated analysis allows to describe partially coherent light from the limit of a few to many modes. Particularly, the beam quality factor, M^2, can be associated with an effective temperature for light beams. This link between optics and thermodynamics allows to describe the beam wavefront based on the mean number of available modes and other macroscopic beam effective parameters, such as the beam width, curvature, and divergence angle. Later, ensembles of beams defined by a fixed M^2 are generated and statistically analyzed. Holography is used to generate the thermodynamically inspired structured light beams, and the statistical analysis of the beam intensity profiles accounts for the retrieval and characterization of the light coherence state. The present discussion can be useful to light propagation in turbulent media, optical systems with imperfections, metasurfaces, and optical communications systems.

Keywords: Structured Light. Optical Thermodynamics. Partially Coherent Light.

RESUMO

O estado de coerência da luz é importante para diversos sistemas ópticos. Tal estado está sujeito a variações que podem ocorrer devido a propagação ou imperfeições presentes no caminho óptico. Apesar de tais variações no estado de coerência serem comuns, medir diretamente tal estado é muitas vezes difícil e a interpretação dessas medidas, complicada, particularmente para feixes com poucos modos. Nesse trabalho, feixes parcialmente coerentes são estudados através de princípios termodinâmicos. Até onde sabemos nossa abordagem é original na literatura e a análise associada permite a descrição de feixes no limite de poucos e muito modos. Em particular, o fator de qualidade do feixe, M^2, pode ser associado a uma temperatura efetiva dos feixes. Essa conexão entre óptica e termodinâmica permite descrever a frente de onda do feixe baseado no número médio de modos disponíveis e outros parâmetros efetivos macroscópicos do feixe, como a largura do feixe, curvature e ângulo de divergência. Posteriormente, ensembles de feixes definidos por um M^2 fixo são produzidos e análises estatísticas sob tais ensembles são realizadas. Holografia é utilizada para gerar feixes estruturados termodinamicamente inspirados e análises estatísticas sob o perfil de intesidade desses feixes possibilitam a recuperação e caracterização do estado de coerência da luz. Essa discussão pode ser útil para estudar luz propagando em meios turbulentos, sistemas ópticos com imperfeições, metasuperfícies e sistemas de comunicação óptico.

Palavras-chaves: Luz Estruturada. Óptica Termodinâmica. Luz Parcialmente Coerente.

LIST OF FIGURES

LIST OF TABLES

LIST OF ABBREVIATIONS AND ACRONYMS

CCD Charged Coupled Device

CSD Cross-Spectral Density

HG Hermite-Gauss

IPCM Interferometric Phase Calibration Method

PBS Polarizing Beam Splitter

RJ Rayleigh-Jeans

SLM Spatial Light Modulator

CONTENTS

1 INTRODUCTION

When light propagates in a free-space optical system, the passage through components or random media can modify some of the beam characteristics. For instance, one of the most significant changes is the modification of the beam modes upon propagation in the optical system. Modes can be added by designed optical elements, such as phase masks, but they are also modified by effects such as aberrated optical elements, propagation through turbid media (GONG et al., 2019), or within biological tissues (HUISKEN; STAINIER, 2009). Thus, studying and understanding multimode beams provide important insights into a variety of optical systems.

Additionally, intrinsic imperfections in an optical system can arise from several effects, such as those due to the fabrication process (PATOUX et al., 2021) or environmental conditions (ANDREWS; PHILLIPS, 2005), (KOROTKOVA, 2014). These wavefront distortions can be critical in some applications, and a significant effort is employed to minimize them. Metasurface fabrication (PAN et al., 2022) and optical communication systems (MILLER, 2019) are examples in which the minimization of these imperfections is crucial to high-performance applications.

Even though aberrations are common in many optical systems, properly accounting for and understanding their influence is often difficult, especially in highly multimode systems. Therefore, an experimental and practical method that allows to understand multimode systems and the influence of optical imperfections can offer new insights into several optical systems of current interest, such as in imaging, spectroscopy, telecommunications, and nonlinear light sources (WRIGHT et al., 2022).

This work proposes a description of light propagating in free-space based on thermodynamic principles. Here, the thermodynamic principles are used as an alternative way of accounting for the presence of spatial modes on light beams. This description is independent of the number of occupied modes and seems appropriate for the analysis of partially coherent light even in the limit of few modes. Particularly, it can be observed that beam imperfections and aberrations continuously increase as more modes are added to the beam wavefront or, alternatively, as the coherence reduces for a given system. Even though such effects can be very small, they can add up and modify the wavefront significantly.

Furthermore, a description that can retrieve direct information regarding the beam propagation can be a useful tool for a variety of optical systems. Particularly, if it can account for small effects that arise from passages through typical optical components as well as scattering

and random media.

This dissertation is organized as follows. Chapter 2 motivates the need for a description to understand changes in the beam wavefront due to random optical elements. Additionally, this chapter defines a free-space thermodynamic description, by linking the beam quality factor, M^2, to an effective temperature. Chapter 3 formalizes the statistical analysis needed to study variations in the beam wavefront. Our proposal seems adequate to characterize partially coherent beams from a few modes up to the many modes regime. Chapter 4 introduces holography principles that will be used in the context of structured light to experimentally generate beams with thermodynamic properties. Finally, Chapter 5, uses structured light to experimentally generate thermodynamic beams and conducts a statistical analysis of the collected data. This analysis not only confirms the theoretical concepts established in the previous chapters but also shows how the proposed description can be experimentally used to study partially coherent light.

2 FREE-SPACE OPTICAL THERMODYNAMICS

The invention of the laser in 1960 had a huge impact on optics. For instance, lasers increased the accessible coherence lengths. While the coherence length of a narrow linewidth atomic vapor lamp, such as the sodium lamp, rarely goes above a few centimeters, it is not uncommon to have lasers with coherence lengths of several meters. The coherence state of a light beam is a central topic in several applications, such as interferometry and holography. While lasers and lamps are often treated as coherent and incoherent sources of radiation, respectively, these idealizations do not correspond to the real world. Both sources are partially coherent, the laser being significantly more coherent than the lamp. This chapter introduces a thermodynamic-inspired description for partially coherent light beams which should be valid for all regimes of coherence. The macroscopic parameters defined, such as the beam width and divergence angle, should be adequate from the perfectly coherent regime up to the completely incoherent regime. This discussion contains novel aspects since the regime of nearly coherent radiation is often neglected in the literature, but it is helpful to understand how real lasers deviate from their ideal properties.

This chapter is organized as follows. First, Section 2.1 contains a brief introduction to optical thermodynamics, going through some of its key characteristics. The following section, Section 2.2, discusses light propagating in random media to motivate the free-space optical thermodynamic description presented in this work. Finally, Section 2.3 shows how such a description can be obtained through ladder operators and defines an effective temperature for an optical system. Which will be further studied and statistically analyzed in Chapter 3, as well as experimentally generated with structured light in Chapter 5.

2.1 BRIEF INTRODUCTION OF OPTICAL THERMODYNAMICS

Optical thermodynamics has emerged as a new way of studying optical systems. The value of such a description relies on the possibility of understanding highly multimode systems with average scalar quantities. Usually, to fully study a system containing N optical modes, one would need to keep track of N dispersion curves and self-phase modulation terms, N^2 cross-phase constants, and N^4 four-wave mixing products (POLETTI; HORAK, 2008). It is not difficult to realize that such an analysis is extremely hard to perform even numerically, if not impossible

in many cases. An optical thermodynamics description not only simplifies the analysis of highly multimode nonlinear systems but also gives additional physical insights regarding the optical system. Hence, this section is dedicated to a brief overview of optical thermodynamics, to better contextualize the analysis further developed in this chapter.

The development of a thermodynamic description for optical systems started with an interest in nonlinear multimode fiber systems, motivated by high-speed communication systems (AMBICHL et al., 2017). Previous works have established non-equilibrium descriptions (PICOZZI et al., 2014), (PICOZZI, 2007), however, an equilibrium description was only recently achieved (WU; HASSAN; CHRISTODOULIDES, 2019). In particular, Wu, Hassan and Christodoulides (2019) have shown that the wavefront properties in the thermal equilibrium regime can be described by equations of state. More interestingly such equations are written in terms of an effective wavefront internal energy, number of modes, and optical power. Explicitly linking the thermodynamic with the optical variables, and being able to extract physical interpretations from such an analysis. Wu, Hassan and Christodoulides (2019) have fully described a highly multimode nonlinear optical system.

From an experimental standpoint, direct measurements of the fine wavefront details of such thermalized systems are difficult to perform. Optical systems are usually subjected to a variety of dissipative phenomena that do not allow the system to reach equilibrium (SURET, 2022). However, as the field of optics develops, so does the experimental possibilities. In the last few years, direct measurements of thermodynamic properties and predictions for fiber optics and guided wave systems have been reported. Namely, the thermalization of an optical system in a Rayleigh-Jeans (RJ) distribution has been experimentally observed (SIDORENKO et al., 2022) (Figure 1). This phenomenon has been theoretically predicted in the context of wave turbulence (PICOZZI et al., 2014), however, the experimental observation has only been possible due to the development of high-quality fibers and high-power laser sources.

Some other remarkable results were recently reported. Ferraro et al. (2024) have also done the first experimental measurements of optical calorimetry in nonlinear multimode fibers. They observed the flow of both temperature and chemical potential, as well as experimentally validated the second law of thermodynamics in fiber-based optical systems showing that the thermodynamical approach can be very useful to describe light propagation in highly multimode optical systems. As another example, Zhang et al. (2024) have recently observed a Bose-Einstein condensation in a fiber-based system. Particularly, they took into account nonlinear dissipative process, and its changes in the entropy flow to provide new insights regarding

Figure 1 – When a highly multimode beam propagates on a multimode optical fiber, the energy exchange between the modes leads to an RJ distribution.

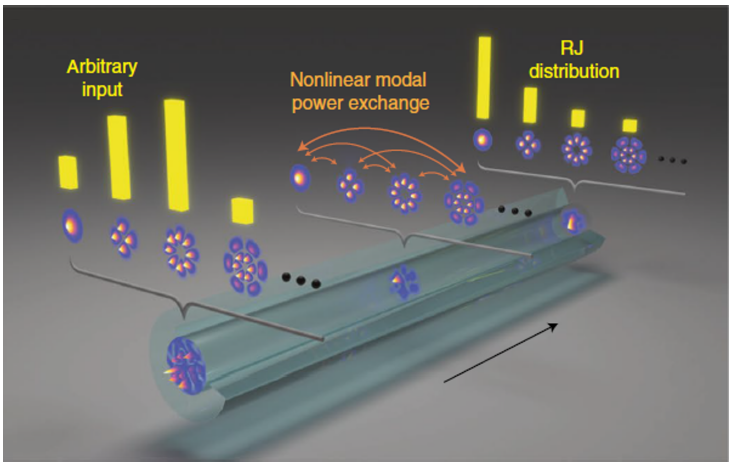

Source: SIDORENKO et al. (2022)

systems described by thermodynamic principles.

Even though optical thermodynamics has been able to explain and explore optical systems in a new way, all the reported results are waveguide-based only. This comes from a theoretical characteristic of the description. As previously stated, upon thermalization the mode distribution matches an RJ distribution (SIDORENKO et al., 2022), which leads to the ultraviolet divergence, similarly as happens in the black-body radiation problem. This cutoff is necessary to regularize the divergence and is indeed naturally obtained in a waveguide-based system. The waveguide confines the system and introduces the cutoff required to avoid the divergence.

When a light beam is propagating in free-space however, there is no natural cutoff. The thermodynamic description previously developed cannot be used. This chapter is dedicated to developing a theoretical apparatus that supports the thermodynamic description of light in free-space. It will be shown that the beam width also introduces a natural cutoff to the system, overcoming the need to force a waveguide-based system.

2.2 PROPAGATION OF LIGHT IN RANDOM MEDIA TO MOTIVATE A FREE-SPACE THERMODYNAMIC DESCRIPTION

When light propagates through free-space, the characteristics of the medium in which it propagates are decisive in promoting changes on the wavefront of the beam. This section is dedicated to studying how the beam parameters change when it propagates through random media. This analysis introduces the basis that motivates the thermodynamic description that

will be developed in Section 2.3.

The analysis starts with light that propagates in a non-absorptive linear medium, which is assumed to exhibit refractive index fluctuations in its volume. To simplify the analysis, this medium can be represented by appropriately placed thin random phase screens (ANDREWS; PHILLIPS; WEEKS, 1997). This description replaces the extended medium with an equivalent model, where light propagates through a homogeneous medium interrupted by a thin phase screen positioned between the source and observation planes. This model has connections with non-absorptive metasurfaces (YU et al., 2011), can represent common optical elements (lenses, mirrors, or prisms), and light propagation through the atmosphere (SHIRAI; DOGARIU; WOLF, 2003). Particularly, the phase screen description can be linked to an operator-based representation of the wavefront (AMARAL et al., 2020) and light propagation in nonlinear materials (PORRAS; ALDA; BERNABEU, 1993). Both representations are connected with the theoretical analysis further developed in this chapter.

First, the paraxial equation is considered to govern the evolution of the electric field $\mathcal{E}$ along the z-axis in a homogeneous medium,

$$i\frac{\partial \mathcal{E}}{\partial z} = H_0\mathcal{E}, \quad H_0 = -\frac{1}{2k}\frac{\partial^2}{\partial x^2}, \tag{2.1}$$

where k is the real wavenumber and only the x-axis is considered. A key conserved quantity is

$$\mathcal{P} = \int |\mathcal{E}|^2\, dx, \tag{2.2}$$

which is proportional to the optical power. Conservation of $\mathcal{P}$ requires that $\frac{\partial \mathcal{P}}{\partial z} = 0$, which is true when

$$\lim_{x\to\pm\infty} \mathcal{E}\frac{\partial}{\partial x}\mathcal{E}^* = 0. \tag{2.3}$$

The conservation of $\mathcal{P}$ implies that the field must be sufficiently localized in the position and angular spectrum, which is satisfied for physical fields over sufficiently large integration regions (PORRAS; ALDA; BERNABEU, 1992).

Since Equation (2.1) is similar to Schrödinger's equation for a free particle, H_0 should be associated with an energy-like conserved quantity. By following a reasoning similar to that used for $\mathcal{P}$, it can be shown that,

$$U = \frac{1}{\mathcal{P}}\int \mathcal{E}^* H_0 \mathcal{E}\, dx, \tag{2.4}$$

is also a conserved quantity under free-space propagation.

U is directly meaningful for a particle, however for a beam propagating in free-space, the effective beam width (W_x), curvature radius (R_x), and divergence angle, (Θ_x) (PORRAS; ALDA; BERNABEU, 1992), are better suited to be used,

$$W_x^2 = \frac{2}{\mathcal{P}} \int (x - \bar{x})^2 |\mathcal{E}|^2 \, dx, \tag{2.5}$$

$$\frac{W_x^2}{R_x} = -\frac{2i}{k\mathcal{P}} \int (x - \bar{x}) \left(\mathcal{E}^* \frac{\partial}{\partial x} \mathcal{E} - \mathcal{E} \frac{\partial}{\partial x} \mathcal{E}^* \right) dx, \tag{2.6}$$

$$\Theta_x^2 = \frac{2}{k^2 \mathcal{P}} \int \left| \frac{\partial \mathcal{E}}{\partial x} \right|^2 dx - \frac{2\bar{p}_x^2}{k^2}, \tag{2.7}$$

where $\bar{x}$ is the beam centroid and $\bar{p}_x/k$, the angle between the beam propagation direction and the optical axis. The effective parameters defined in Equations (2.5)-(2.7) can be evaluated at any z-plane and are directly related to the second-order intensity moments (BEKSHAEV, 2006).

There are two conserved quantities up to the second-order intensity moments for free-space propagation:

1. The divergence angle (Θ_x) remains constant upon free-space propagation. An integration by parts along x in Equation (2.7) can be used to show that

$$\Theta_x^2 = \frac{4U}{k} - \frac{2\bar{p}_x^2}{k^2}. \tag{2.8}$$

2. The square of the beam quality factor M_x^2 is invariant upon translation (BEKSHAEV, 2006), (PORRAS; ALDA; BERNABEU, 1992). Since it is related to the product between the minimum beam width and the divergence angle,

$$M_x^4 = \frac{k^2}{4} \left[\Theta_x^2 W_x^2 - \left(\frac{W_x^2}{R_x} \right)^2 \right]. \tag{2.9}$$

M_x^2 is known as the beam propagation, or beam quality factor, and satisfies $M_x^2 \geq 1$. The equality is verified for Gaussian beams, while values of $M_x^2 > 1$ indicate the presence of higher-order modes on the beam.

With these notions established, the next step is to analyze how a thin optical element changes these beam parameters. A non-absorptive thin optical element can be represented by a phase screen with the transmission coefficient $S = e^{i\phi}$, and its effects on an initial field $\mathcal{E}_0 = |\mathcal{E}_0| e^{i\Phi}$ is

$$\mathcal{E}_1 = S\mathcal{E}_0 = |\mathcal{E}_0| e^{i(\phi + \Phi)}, \tag{2.10}$$

where $\mathcal{E}_1$ is the electric field after the phase screen, $|\mathcal{E}_0|$ and Φ are the initial field amplitude and phase, respectively. For simplicity, here is considered that $\bar{x} = \bar{p}_x = 0$, which means that

the beam propagates along the optical axis. Additionally, since S is a pure phase mask, it is true that $|\mathcal{E}_1|^2 = |\mathcal{E}_0|^2$, meaning that the beam transmission through S does not change $\mathcal{P}$ and W_x^2.

Now, the pairs of quantities $(R_{x,0}, \Theta_{x,0})$ and $(R_{x,1}, \Theta_{x,1})$ are defined as the effective curvature and divergence angle before and after S, respectively. Then, it can be shown that

$$\frac{W_x^2}{R_{x,1}} = \frac{4}{k\mathcal{P}} \int x \frac{\partial \phi}{\partial x} |\mathcal{E}_0|^2 \, dx + \frac{W_x^2}{R_{x,0}}, \tag{2.11}$$

$$\Theta_{x,1}^2 = \frac{2}{k^2\mathcal{P}} \int \left[\left(\frac{\partial \phi}{\partial x} \right)^2 + 2 \frac{\partial \phi}{\partial x} \frac{\partial \Phi}{\partial x} \right] |\mathcal{E}_0|^2 \, dx + \Theta_{x,0}^2 \tag{2.12}$$

$$= \frac{2}{k^2\mathcal{P}} \int \left\{ \left[\frac{\partial}{\partial x} (\phi + \Phi) \right]^2 |\mathcal{E}_0|^2 + \left| \frac{\partial |\mathcal{E}_0|}{\partial x} \right|^2 \right\} dx, \tag{2.13}$$

which implies that the curvature and divergence angle will be modified for a spatially varying ϕ.

With these concepts, it is possible to evaluate a series of changes in a light beam associated with different field and phase mask characteristics.

2.2.1 Light propagating in random media

When a beam propagates through a medium with strong phase fluctuations, such that ϕ is uniformly distributed, depends only on the material, and is completely uncorrelated with the beam phase Φ. This situation represents ordinary light transmission through scattering materials such as biological tissues, colloids, or turbulent fluids. The ensemble average is $\left\langle \frac{\partial \phi}{\partial x} \right\rangle = 0$, and

$$\left\langle \frac{W_x^2}{R_{x,1}} \right\rangle = \left\langle \frac{W_x^2}{R_{x,0}} \right\rangle, \tag{2.14}$$

$$\left\langle \Theta_{x,1}^2 \right\rangle = \frac{2}{k^2\mathcal{P}} \int \left\langle \left(\frac{\partial \phi}{\partial x} \right)^2 \right\rangle |\mathcal{E}_0|^2 \, dx + \left\langle \Theta_{x,0}^2 \right\rangle. \tag{2.15}$$

Since $\Theta_x^2 \propto U$, this can also be written as $U_1 = U_0 + |\Delta U|$. And, W_x remains constant across S, from 2.9 one can infer that,

$$M_{x,1}^4 = M_{x,0}^4 + \frac{W_x^2}{2\mathcal{P}} \int \left\langle \left(\frac{\partial \phi}{\partial x} \right)^2 \right\rangle |\mathcal{E}_0|^2 \, dx. \tag{2.16}$$

Which means that $M_{x,1}^4$ necessarily increases after being transmitted by S. This can be understood as higher-order modes being introduced to the wavefront due to the random phase

mask associated with S. This transformation can be used to describe weakly and strongly turbulent media by using the appropriate phase function, such as for light propagation in the atmosphere (ANDREWS; PHILLIPS; WEEKS, 1997).

2.2.2 Light correlated with phase introduced by random media

The control of light propagation in random media is an important challenge for many applications. To cite one, wavefront shaping has been recently used to compensate for the scattering-induced phase distortions introduced by a random medium (HUA et al., 2024).

The ensemble average must be performed more carefully when ϕ and Φ are strongly correlated. In the extreme case of phase-conjugation, where $\Phi = -\phi$, it is true that

$$W_x^2/R_{x,1} = 0, \tag{2.17}$$

and the divergence angle assumes a minimal value independent of any randomness in ϕ. Equation 2.13 shows that a phase conjugated field has a minimum divergence which depends only on the beam amplitude profile,

$$\Theta_{x,min}^2 = \frac{2}{k^2\mathcal{P}} \int \left| \frac{\partial |\mathcal{E}_0|}{\partial x} \right|^2 dx. \tag{2.18}$$

Now consider a simple correlation between the field and the phase introduced by the random media, such that $\Phi = u\phi$, where u is a real constant. From Equations (2.11) and (2.13), it possible to obtain

$$\frac{W_x^2}{R_{x,1}} = (1+u)\frac{W_x^2}{R_{x,0}}, \tag{2.19}$$

$$\Theta_{x,1}^2 = (1+u)^2 \left(\Theta_{x,0}^2 - \Theta_{x,min}^2\right) + \Theta_{x,min}^2, \tag{2.20}$$

whose substitution in Equation (2.9) allows the comparison between the initial and final propagation factors as

$$M_{x,1}^4 = (1+u)^2 M_{x,0}^4 - \frac{k^2 W_x^2 \Theta_{x,min}^2}{4}(u^2+2u). \tag{2.21}$$

Equations (2.19)-(2.21) are simpler to understand in the limit of several initial and final modes, where

$$\Theta_{x,0}^2, \Theta_{x,1}^2 \gg \Theta_{x,min}^2. \tag{2.22}$$

In this situation, both $\Theta_{x,1}^2$ and $M_{x,1}^4$ become proportional to $(1+u)^2$, and their magnitudes decrease after the phase mask only when $-2 < u < 0$. Complementary, $\Theta_{x,1}^2$ and $M_{x,1}^4$ increase

either when $u > 0$ or $u < -2$. This means that, for a field correlated with the random medium, the energy transformation becomes

$$U_1 = U_0 + \Delta U \geq \frac{k}{4}\Theta^2_{x,min}. \tag{2.23}$$

Therefore, notice that a wavefront correlated with the random media allows to have $\Delta U > 0$ or $\Delta U < 0$, such the energy may increase or decrease (respecting the lower bound introduced by θ_{min}).

2.2.3 Multiple passages through thin random media

Now it will be considered the case where the beam passes through the phase screen multiple times, as in a laser cavity. Phase variations, ϕ, can arise from effects such as imperfections in optical components, mechanical vibrations, temperature gradients, or current self-distribution in laser diodes. In the stationary cavity regime, Section 2.2.1 suggests that when the wavefront Φ is uncorrelated with the phase ϕ introduced by the random medium, then U increases for each cavity roundtrip.

This behavior is not consistent with a stationary field profile and implies that Φ and ϕ must exhibit some degree of correlation. The stationary field behavior within a cavity requires that some optical elements contribute with $\Delta U > 0$, while others must impose $\Delta U < 0$. Stability after a single roundtrip requires $\sum_j \Delta U_j = 0$, where ΔU_j corresponds to the j-th optical element encountered in a roundtrip. This process can be considered as one in which the wavefront effective energy is not conserved at each small process, but has a well defined stationary value after circulation several times within the cavity.

2.3 DEFINITION OF TEMPERATURE-LIKE PARAMETER TO A LIGHT BEAM

By utilizing statistical mechanics principles, it is possible to define a temperature-like parameter that characterizes the distribution of spatial modes in an arbitrary beam. That is useful for retrieving additional information about an arbitrary optical system, as well as to characterize imperfections added to a given experimental setup as discussed in Section 2.2, using only a snapshot of the beam wavefront. The following section describes how an effective temperature of a beam can be defined and the physical meaning behind such a parameter in an optical system.

To start this analysis, a complete basis of modes can describe the wavefront of a beam. Since the Hermite-Gauss (HG) modes are directly connected with the laser modes (KOGELNIK; LI, 1966), they are useful for describing the beam properties when propagating in free-space. An HG beam, has a finite width w_0 and can be related with the quantum harmonic oscillator (NIENHUIS; ALLEN, 1993). For a beam propagating in free-space, w_0 is a free parameter. To specify it, the relation between w_0 and the intensity beam moments up to second order (BEKSHAEV, 2006) is used here. The following analysis considers only the propagation in the z-direction, the analogous results for more dimensions can be found at (NIENHUIS, 2017).

To perform a coherent-mode representation (OSTROVSKY, 2006) of a beam propagating along the z-axis such that $z = 0$, the wavefront envelope is defined as

$$\mathcal{E}(x) = \sum_{n=0}^{\infty} a_n \psi_n(x), \tag{2.24}$$

where a_n is the complex amplitude of the normalized mode $\psi_n(x)$, and the normalization is

$$\sum_{n=0}^{\infty} |a_n|^2 = 1. \tag{2.25}$$

For the HG basis, the mode can be written as

$$\psi_n(x) = \left(\frac{2}{\pi w_0^2}\right)^{1/4} \frac{1}{\sqrt{2^n n!}} H_n\left(\frac{\sqrt{2}x}{w_0}\right) e^{-\frac{x^2}{w_0^2}}. \tag{2.26}$$

Furthermore, it is possible to define $\overline{x}$ and $\overline{p_x}/k$ as the first-order moments that represent the beam centroid and mean angle relative to the propagation axis, respectively. In terms of $\mathcal{E}(x)$, the average of the first-order moments are

$$\overline{x} = \int dx\, \mathcal{E}^*(x) x \mathcal{E}(x), \tag{2.27}$$

and

$$\overline{p_x} = \int dp_x\, \tilde{\mathcal{E}}^*(p_x) p_x \tilde{\mathcal{E}}(p_x), \tag{2.28}$$

where $\tilde{\mathcal{E}}(p_x)$ corresponds to the Fourier transform of $\mathcal{E}(x)$. The following section is dedicated to obtaining the first and second-order moments for an HG basis.

2.3.1 Calculation of first and second-order moments

The following calculation is strongly inspired in the formalism introduced in (NIENHUIS; ALLEN, 1993), $\hat{x}, \hat{p}$ as operators and their commutator satisfying $[\hat{x}, \hat{p}] = i$ are defined. For an

arbitrary wavefront state at a plane z, $|\mathcal{E}(z)\rangle$, the paraxial equation in free-space is

$$-i\frac{d}{dz}|\mathcal{E}(z)\rangle = \hat{H}_0|\mathcal{E}(z)\rangle, \quad \hat{H}_0 = \frac{\hat{p}^2}{2k}, \tag{2.29}$$

where k is the wavenumber, $\hat{p} \equiv -i\frac{\partial}{\partial x}$, $\frac{\hat{p}^2}{2k} \equiv -\frac{1}{2k}\frac{d^2}{dx^2}$, and the operator $\hat{H}_0$ corresponds to the linear diffraction term.

The general solution for the free-space propagation problem in a Heisenberg operator representation is

$$|\mathcal{E}(z)\rangle = \hat{U}(z)|\mathcal{E}(0)\rangle, \quad \hat{U}(z) = e^{\frac{i}{2k}\hat{p}^2 z}. \tag{2.30}$$

By direct analogy with the classical harmonic oscillator, a characteristic transverse scale b is defined to generate a set of localized modes

$$\hat{H} = \frac{\hat{p}^2}{2k} + \frac{k}{2}\frac{\hat{x}^2}{b^2}, \tag{2.31}$$

where at this step b is a free-parameter.

Now, the ladder operators are introduced at the $z = 0$ plane and defined as

$$\hat{a}(0) = \sqrt{\frac{k}{2b}}\left(\hat{x} + i\frac{\hat{p}}{k}b\right), \; \hat{a}^\dagger(0) = \sqrt{\frac{k}{2b}}\left(\hat{x} - i\frac{\hat{p}}{k}b\right), \tag{2.32}$$

and the following identities hold

$$[\hat{a}(0), \hat{a}^\dagger(0)] = 1, \quad \hat{a}^\dagger(0)\hat{a}(0) + \frac{1}{2} = b\hat{H}. \tag{2.33}$$

The operators in Equation (2.32), defined at $z = 0$, can produce a complete basis of propagating HG modes. The relations in Equation (2.33) are still valid when using the Heisenberg operator picture, which allows the verification of Equation (2.33) upon propagation at an arbitrary z-plane. To alter from the Schrödinger picture to the Heisenberg picture, the following transformation is used

$$\hat{O}_H(z) = \hat{U}^\dagger(z)\hat{O}_S\hat{U}(z), \tag{2.34}$$

where $\hat{O}_S$ is the Schrödinger picture operator and $\hat{O}_H(z)$ is the Heisenberg picture operator. Particularly, this transformation for $\hat{x}$ and $\hat{p}$ can be written as

$$\hat{x}(z) = \hat{U}^\dagger(z)\hat{x}\hat{U}(z) = \hat{x} - \frac{\hat{p}}{k}z, \tag{2.35}$$

$$\hat{p}(z) = \hat{U}^\dagger(z)\hat{p}\hat{U}(z) = \hat{p} \tag{2.36}$$

Which when applied to Equation (2.32), can describe the propagation of the beam in the z-direction,

$$\hat{a}(z) = \sqrt{\frac{k}{2b}}\left[\hat{x} - \frac{\hat{p}}{k}(z - ib)\right], \tag{2.37}$$

$$\hat{a}^\dagger(z) = \sqrt{\frac{k}{2b}}\left[\hat{x} - \frac{\hat{p}}{k}(z + ib)\right]. \tag{2.38}$$

Retrieving the identities in Equation (2.33), that are now valid at all z-planes,

$$[\hat{a}(z), \hat{a}^\dagger(z)] = 1, \quad \hat{a}^\dagger(z)\hat{a}(z) + \frac{1}{2} = b\hat{H}(z). \tag{2.39}$$

In an optical system, $\hat{x}(z)$ and $\hat{p}(z)/k$ correspond to the beam coordinate and angle relative to the propagation axis, respectively. Such a connection between wave operators and geometrical opticals were previously established, and can be found for example at (NAZARATHY; SHAMIR, 1982) and (NAZARATHY; SHAMIR, 1982).

The commutator in Equation (2.39) determines that the spectrum of the number operator $\hat{n}(z) = \hat{a}^\dagger(z)\hat{a}(z)$ is composed of natural numbers and that it is preserved upon propagation, $\hat{n}(z)|n\rangle = n|n\rangle$. The raising and lowering operators acts on $|n\rangle$ as

$$\hat{a}(z)|n\rangle = \sqrt{n}|n-1\rangle, \quad \hat{a}^\dagger(z)|n\rangle = \sqrt{n+1}|n+1\rangle. \tag{2.40}$$

The lowest eigenvalue is $\hat{n}|0\rangle = 0|0\rangle = 0$, which defines the fundamental Gaussian mode on this basis. The condition $\hat{a}(z)|0\rangle = 0$ establishes the value of b as

$$b = z_0 = \frac{kw_0^2}{2}, \tag{2.41}$$

for a mode with a waist w_0 and where z_0 is the Rayleigh length of the fundamental mode. $\hat{a}(z)|0\rangle = 0$ also establishes a complex beam parameter,

$$q(z) = z - ib = z - iz_0. \tag{2.42}$$

With the ladder operators, an arbitrary wavefront state $|\mathcal{E}(z)\rangle$ is defined anywhere as

$$|\mathcal{E}(z)\rangle = \sum_{n=0}^{\infty} a_n |n(z)\rangle, \quad |n(z)\rangle = \frac{\left[\hat{a}^\dagger(z)\right]^n}{\sqrt{n!}}|0(z)\rangle. \tag{2.43}$$

For the beam's transverse operators, it can be shown from Equations (2.37) and (2.38) that

$$\hat{a}(z) = \frac{1}{w_0}\left[\hat{x} - \frac{\hat{p}}{k}q(z)\right], \tag{2.44}$$

$$\hat{a}^\dagger(z) = \frac{1}{w_0}\left[\hat{x} - \frac{\hat{p}}{k}q^*(z)\right], \tag{2.45}$$

$$\hat{x}(z) = \frac{w_0}{2}\left[\hat{a}(z) + \hat{a}^\dagger(z)\right] + \frac{\hat{p}(z)}{k}z, \tag{2.46}$$

$$\hat{p}(z) = \frac{1}{iw_0}\left[\hat{a}(z) - \hat{a}^\dagger(z)\right]. \tag{2.47}$$

Since the analysis does not change significantly upon propagation, $z = 0$ is considered from this point. The integrals in Equation (2.27) and (2.28), can be calculated directly and to write them in terms of operators, some algebra is needed, as it follows,

$$\overline{x} = \langle \mathcal{E}|\hat{x}|\mathcal{E}\rangle = w_0 \Re(K_x), \quad \overline{p} = \langle \mathcal{E}|\hat{p}|\mathcal{E}\rangle = \frac{2}{w_0}\Im(K_x), \tag{2.48}$$

where

$$K_x = \langle \mathcal{E}|\hat{a}|\mathcal{E}\rangle = K_x = \sum_{n=0}^{\infty} \sqrt{n+1} a_n^* a_{n+1} \tag{2.49}$$

The first-order moments, $\overline{x}$ and $\overline{p}$, are related to the ray-like properties of the beam. The second-order moments are associated with effective wavefront parameters and their propagation. $\overline{x^2}$ is related to the effective beam width at the reference plane, while $\overline{x^2(z)}$ generalizes it to arbitrary z planes. Separating $\overline{x^2(z)}$ in powers of z, two other operator combinations can be considered, $\overline{(\hat{x}\hat{p} + \hat{p}\hat{x})/k}$, which is related to an effective curvature radius, and $\overline{\hat{p}^2/k^2}$ which is related to an effective divergence angle. Using Equations (2.46) and (2.47) it can be shown that

$$\overline{\hat{x}^2} = \langle \mathcal{E}|\hat{x}^2|\mathcal{E}\rangle = \frac{w_0^2}{4}\left[M_x^2 + 2\Re\left(L_x\right)\right], \tag{2.50}$$

$$\overline{\hat{p}^2} = \langle \mathcal{E}|\hat{p}^2|\mathcal{E}\rangle = \frac{1}{w_0^2}\left[M_x^2 - 2\Re\left(L_x\right)\right], \tag{2.51}$$

$$\overline{\hat{x}\hat{p} + \hat{p}\hat{x}} = \langle \mathcal{E}|\hat{x}\hat{p} + \hat{p}\hat{x}|\mathcal{E}\rangle = 2\Im\left(L_x\right), \tag{2.52}$$

$$L_x = \langle \mathcal{E}|\hat{a}^2|\mathcal{E}\rangle = \sum_{n=0}^{\infty} \sqrt{(n+2)(n+1)} a_n^* a_{n+2}, \tag{2.53}$$

$$M_x^2 = \langle \mathcal{E}|2\hat{a}^\dagger\hat{a} + 1|\mathcal{E}\rangle = 2\sum_{n=0}^{\infty}\left(n + \frac{1}{2}\right)|a_n|^2. \tag{2.54}$$

from the equations above, one can observe that the first and second-order moments depend on three parameters K_x, L_x, and M_x. However, only M_x is non-zero on average when the phases between a_n and a_m vary randomly, since $< a_n^* a_{n+1} >= 0$ and $< a_n^* a_{n+2} >= 0$. Therefore, up to second-order in the beam moments, there are only two parameters to describe the beam, w_0 and M_x.

2.3.2 Definition of a temperature-like parameter for a beam

Defining the experimental beam width (ISO Standard 11146-1:2021, 2021) as

$$W_x = w_0\sqrt{M_x^2}, \tag{2.55}$$

which specify W_x the geometrical parameter of the beam, while M_x^2 accounts for the incoherent properties of the beam wavefront. M_x^2 (SIEGMAN, 1993) is the beam quality factor or beam propagation parameter, its properties account for the presence of higher spatial modes other than the pure Gaussian on a beam wavefront. M_x^2 vary from 1 to ∞, with 1 being a purely Gaussian beam, and as the value of M_x^2 grows, so does the presence of higher spatial modes, which increases the presence of speckle-like patterns on the beam wavefront (Figure 2).

Figure 2 – Different values of M_x^2. (a) An almost purely Gaussian beam. (b) The presence of higher spatial modes gives the wavefront a speckle-like appearance.

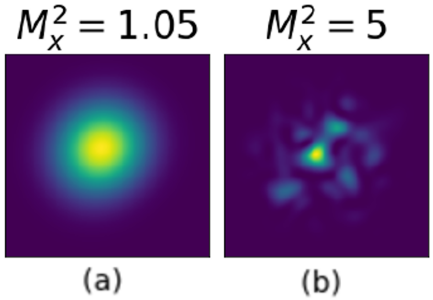

Source: Author (2024)

Since M_x^2 is defined by a sum of infinite amplitudes a_n, there are infinite possibilities for setting this sum. Among such sums, there is one in which the a_n requires a minimal amount of information to be completely specified. To account for the minimal information wanted to specify such a set of a_n, an entropy-like quantity is defined and subjected to the constraints of a fixed M_x^2 and normalization, which gives

$$Q = -\sum_n |a_n|^2 \log |a_n|^2 + \gamma \left(1 - \sum_n |a_n|^2\right) + \beta \left[M_x^2 - 2\sum_n \left(n + \frac{1}{2}\right) |a_n|^2\right], \tag{2.56}$$

where γ and β are Lagrange multipliers (Wu et al. (2020)). Equation 2.56 is the Gibbs' entropy subjected to the constraints of a normalized a_n and a fixed M_x^2, which multiplies the Lagrange multiplier γ and β, respectively. Gibbs' entropy is used instead of Boltzmann's entropy because the process which leads to thermalization, such as the beam within a laser cavity, does not maintain the wavefront energy constant, but is more similar to a process in which the temperature is kept constant.

This entropy is then maximized, leading to

$$|a_n| = Nc^n, \tag{2.57}$$

where $N = \exp\left[-(\alpha + \beta + 1)/2\right]$ and $c = \exp(-\beta)$. The normalization constraint in Equation (2.56), allows to write the relation $N^2 = 1 - c^2$, while the M_x^2 constraint can be used to obtain c^2 and N^2 in terms of M_x^2,

$$N^2 = \frac{2}{M_x^2 + 1} = 1 - e^{-2\beta}, \tag{2.58}$$

$$c^2 = \frac{M_x^2 - 1}{M_x^2 + 1} = e^{-2\beta}. \tag{2.59}$$

Since the Lagrange multiplier β is related to the inverse of a temperature-like quantity, it is possible to write

$$\beta = \frac{1}{T_x} = \frac{1}{2} \ln \left(\frac{M_x^2 + 1}{M_x^2 - 1} \right). \tag{2.60}$$

Equation 2.60 states that there is a direct relation between T_x and M_x^2 (Figure 3). This implies that a beam with a specific M_x^2 also has an effective temperature T_x. And not only that, from Equation (2.55), M_x^2 is directly linked to the beam geometrical parameter, or beam waist W_x. The relation between M_x^2 and T_x also implies that as long as the beam has a finite width, which is true for all real beams, an effective temperature T_x can also be defined.

Figure 3 – Relation between the beam quality factor, M_x^2 and an effective temperature T_x of the beam.

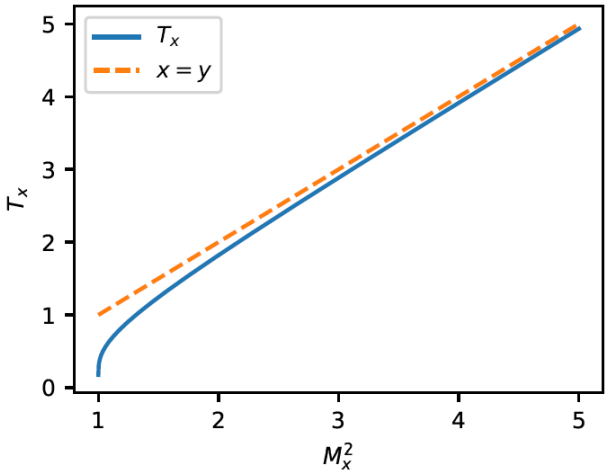

Source: Author (2024)

T_x can also be understood as a measurement of the occupancy of spatial modes of a beam. A "cold" beam ($T_x \approx 0$ or $M_x^2 \approx 1$) means an almost purely Gaussian beam. While a "hot" beam ($0 \ll T_x \approx M_x^2$), has more modes occupied. As the M_x^2 goes higher, so does the occupancy of higher spatial modes.

The occupancy of the spatial modes can also be observed through the amplitudes a_n,

$$|a_n|^2 = 2 \frac{(M_x^2 - 1)^n}{(M_x^2 + 1)^{n+1}}. \tag{2.61}$$

When $M_x^2 \leq 2$, a "cold" beam is characterized, and the lower spatial modes dominate the mode occupancy. As M_x^2 increases so does the presence of higher spatial modes (Figure 4).

Figure 4 – The mode occupancy in terms of $|a_n|^2$. (a) Represents the mode occupancy of the four lowest modes, showing that for $M_x^2 \leq 2$ the beam is almost a pure Gaussian beam. (b) Shows the mode occupancy in terms of M_x^2.

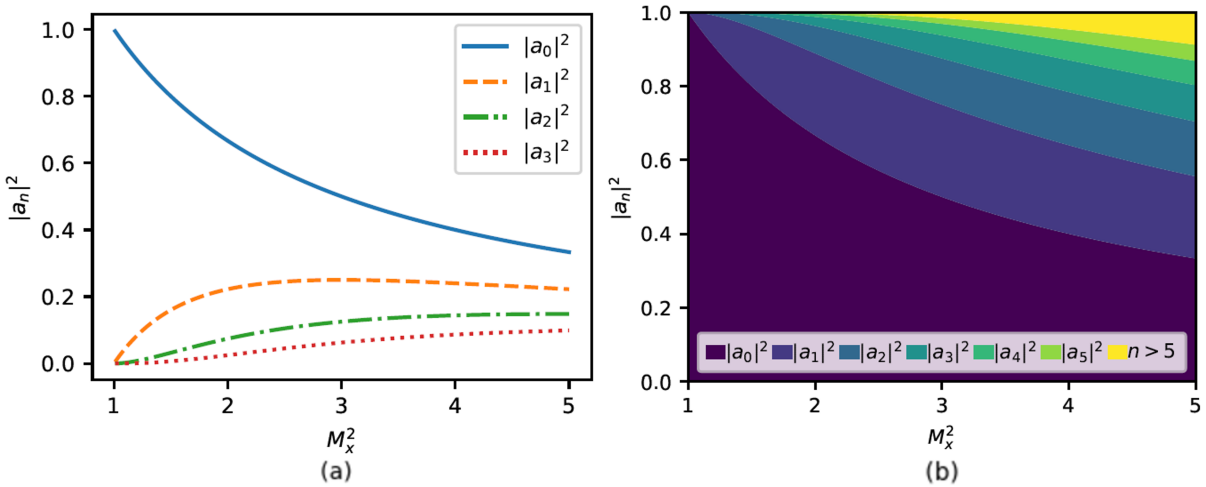

Source: Author (2024)

3 STATISTICAL ANALYSIS OF AN BEAM ENSEMBLE WITH A FIXED $\mathbf{M_x^2}$

In the Section 2.3, the use of ladder operators and an entropy-like quantity allows to define an effective temperature for a light beam. This implies that a given occupation of spatial modes defines an effective temperature T_x, precisely. This means that for a given T_x, the series which represents the spatial modes can be truncated. For a specific T_x, only a finite number of n modes are relevant, higher modes than n can be disregarded. However, while $|a_n|^2$ is determined for a given temperature, different combinations of $a_n = |a_n|e^{i\phi_n}$ can be used to represent a given T_x since ϕ_n remains as free parameters.

The following section will focus on studying how statistical analysis of the beam wavefront allows the gain of information regarding the beam propagation. Since a variety of a_n can characterize a specific T_x. An ensemble of beams defined by its T_x can be statistically analyzed and information regarding the beam propagation is uncovered. Moreover, through the analysis of the beam intensity profile one can also infer the effective beam temperature T_x and beam quality factor M_x^2, through connections with the Gaussian Schell-model. Finally, the analysis of the ensembles can be theoretically predicted through connections with the Fisher transformation. This shows that a system with a random variable presents different statistical signatures that account for different ensembles, here fixed by its T_x or M_x^2.

3.1 RETRIEVAL OF BEAM QUALITY FACTOR M_x^2 THROUGH THE GAUSSIAN SCHELL-MODEL

While the experimental retrieval of the complete beam wavefront is a difficult task in an arbitrary optical system, the beam effective width and divergence angle are relatively easy to retrieve, requiring only a snapshot of the beam profile (JORGE et al., 2014). Typically the snapshot provides information on the intensity profile of the light beam, allowing the measurement of the effective beam width W_x, which supplies information regarding the beam quality factor M_x^2 as well (ISO Standard 11146-1:2021, 2021), Equation (2.55). However, a single snapshot cannot provide complete information about the beam propagation (CRISPIM et al., 2023). In these conditions, statistical analysis of the wavefront can be a useful tool to access information regarding the beam propagation. The following section shows how the well-established Gaussian Schell-model can be linked with the analysis in Section 2.3, and utilized to extract

the effective temperature T_x of a thermodynamic beam light source.

The statistical properties of partially coherent light can be described by the Cross-Spectral Density (CSD), which for a stationary monochromatic light at z=0, can be written as

$$W(x_1, x_2) = \langle \mathcal{E}^*(x_1)\mathcal{E}(x_2)\rangle \tag{3.1}$$

$$= \sqrt{I(x_1)I(x_2)}\mu(|x_1 - x_2|), \tag{3.2}$$

where $I(x_i)$ is the spectral intensity at x_i and $\mu(|x_1 - x_2|)$ is the normalized complex degree of spatial coherence (MANDEL; WOLF, 1976), and indicates the coherence or the correlation between the fields evaluated at two points x_1 and x_2, which should be 1 at $x_1 = x_2$. Particularly, it is possible to obtain the spectral density I_x of light from the CSD,

$$W(x, x) = I(x). \tag{3.3}$$

It is possible to determine Equation (3.1) for an arbitrary light source, and then obtain its spectral density $I(x)$ and degree of spatial coherence $\mu(|x_1 - x_2|)$ through Equation (3.2), (STARIKOV; WOLF, 1982).

Utilizing the description of a light beam shown in Section 2.3, one can use Equations 2.24 and 3.1 to write,

$$W(x_1, x_2) = \sum_{m,n=0}^{\infty} \langle a_m^* a_n \rangle \, \psi_m^*(x_1)\psi_n(x_2). \tag{3.4}$$

The random relative phases are uniformly distributed, which implies that $\langle a_m^* a_n\rangle = |a_n|^2\delta_{m,n}$. By taking Equation (3.4), the bilinear generating equation (STARIKOV; WOLF, 1982), used to generate polynomials, here HG polynomials, can be written as

$$\sum_{n=0}^{\infty} H_n(x)H_n(y)\frac{t^n}{n!} = \frac{\exp\left[y^2 - \frac{(y-2xt)^2}{1-4t^2}\right]}{\sqrt{1-4t^2}}, \tag{3.5}$$

where $x = \sqrt{2}x_1/w_0$, $y = \sqrt{2}x_2/w_0$ and $t = c^2/2$. Putting together Equations (2.26) with (3.5), the sum in Equation (3.4) can be performed. Finally, it can be verified that

$$1 - 4t^2 = 1 - c^4 = M_x^2 N^4, \tag{3.6}$$

such the CSD for the thermodynamic beam can be written as

$$W(x_1, x_2) = \left[\frac{2}{\pi W_x^2}\right]^{1/2} \exp\left[\frac{(x_2^2 - x_1^2)M_x^2}{W_x^2} - \frac{2}{W_x^2}\frac{1}{N^4}\left(x_2 - x_1 c^2\right)^2\right]. \tag{3.7}$$

where N was is given by Equation (2.58).

To show explicitly how the CSD can describe the properties of the thermodynamic beam, the relation in Equation (2.60), can be used to express the beam quality factor M_x^2 as a function of the effective temperature T_x,

$$M_x^2 = \coth(1/T_x). \tag{3.8}$$

Which allows to write Equation (3.7), as

$$W(x_1, x_2) = \left[\frac{2}{\pi W_x^2}\right]^{1/2} \exp\left[\frac{(x_2^2 - x_1^2)}{W_x^2}\coth(1/T_x) \; - \frac{2}{W_x^2}\left(\frac{x_2 - x_1 e^{-2/T_x}}{1 - e^{-2/T_x}}\right)^2\right]. \tag{3.9}$$

Two extreme thermodynamic limits ($T_x \to 0$ and $T_x \to \infty$) can be directly obtained from Equation (3.9):

1. In The "cold" beam regime, the expected Gaussian behavior is retrieved as $T_x \to 0$,

$$W(x_1, x_2) = \left[\frac{2}{\pi W_x^2}\right]^{1/2} \exp\left[-\frac{(x_1^2 + x_2^2)}{W_x^2}\right]. \tag{3.10}$$

2. In the limit that $T_x \to \infty$,

$$W(x_1, x_2) = \left[\frac{2}{\pi W_x^2}\right]^{1/2} \exp\left[-\frac{(x_2 - x_1)^2}{2W_x^2}T_x^2\right] \to 0. \tag{3.11}$$

For the spectral density $I(x) = W(x, x)$, it is possible to write

$$I(x) = \sum_{n=0}^{\infty} |a_n|^2 |\psi_n(x)|^2 \tag{3.12}$$

$$= \left(\frac{2}{\pi W_x^2}\right)^{1/2} \exp\left[-\frac{2x^2}{W_x^2}\right], \tag{3.13}$$

so that $I(x)$ is a T_x-independent Gaussian-shaped beam. Also, from Equations (3.2) and (3.13) it is possible to write

$$\mu(|x_1 - x_2|) = \exp\left[-\frac{M_x^4 - 1}{2W_x^2}(x_1 - x_2)^2\right], \tag{3.14}$$

which, together with Equation (3.13), defines a 1D Gaussian Schell-model field.

Some important physical analysis can be inferred from the previously displayed discussion. First, the coherence width σ_μ is proportional to the beam width and satisfies

$$\sigma_\mu^2 = \frac{W_x^2}{M_x^4 - 1}. \tag{3.15}$$

For a "cold" beam ($T_x \approx 0$ and $M_x^2 \approx 1$), such that

$$M_x^4 - 1 \approx 2(M_x^2 - 1), \tag{3.16}$$

and the coherence width is much larger than the physical beam. While for a "hot" beam ($T_x \approx M_x^2 \gg 1$), the coherence width σ_μ goes with W_x/T_x, which accounts for the speckle-like structures in this regime. This implies that a measure of the transverse beam coherence width can be used to determine the temperature for "hot" beams. The transition from fully to partially coherent fields occurs around $\sigma_\mu = W_x$, or $M_x^2 = \sqrt{2}$.

Finally, the mode structure indicated by Equation (2.61) is exactly the same as the one obtained from Starikov and Wolf (1982), given a proper parameter adjustment. Therefore, the thermodynamic description of free-space light beams is directly linked with the well-established theory of partially coherent beams. Particularly, the present description uses M_x^2 to define the degree of coherence, which allows retrieval of information for coherent and incoherent sources and introduces the transition between both regimes at $M_x^2 = \sqrt{2}$.

A snapshot of the beam wavefront allows the measurement of the beam intensity profile, while with the CSD the information is obtained through correlations in the beam. Therefore, additional information about the optical system can be encoded in the beam intensity profile. Such information can be retrieved through statistical analysis of the properties of the beam intensity profile. Figure 5 shows how the beam intensity profile can vary for a fixed M_x^2, indicating that a statistical analysis could be useful when the beam snapshot is available.

Figure 5 – Intensity profiles $I_\alpha(x)$ (blue lines) compared to the ensemble mean $I(x)$ (yellow filled-region). While the columns represent a fixed M_x^2, characterized by its mode occupancy (Equation (2.61)). The lines represent different ways in which such a mode occupancy appears in the intensity profile $I_\alpha(x)$.

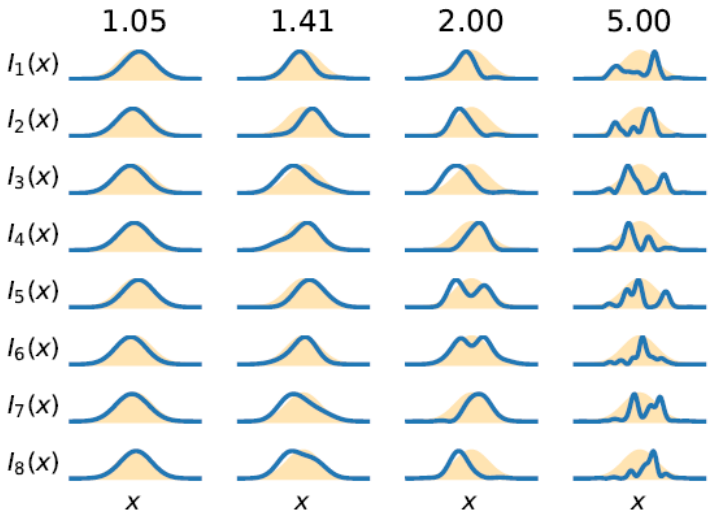

Source: Author (2024)

To start the analysis the following product is considered

$$\mathcal{E}^*(x)\mathcal{E}(x) = \sum_{m,n=0}^{\infty} a_m^* a_n \psi_m^*(x)\psi_n(x) \tag{3.17}$$

$$= \sum_{n=0}^{\infty} |a_n|^2 |\psi_n(x)|^2 + \sum_{\substack{m,n=0 \\ m\neq n}}^{\infty} a_m^* a_n \psi_m^*(x)\psi_n(x). \tag{3.18}$$

Here, it is worth mentioning that

$$a_m^* a_n = |a_m||a_n| \exp(i\phi_n - i\phi_m), \tag{3.19}$$

which shows that the mode phases appear only as phase differences. Then the averages must be performed over phase differences, and not over the phases themselves. Also, the double sum in Equation (3.18) has both the terms i, j, and j, i summed. So, for a set of real basis functions $\psi_n(x)$, the imaginary parts of the complex exponentials cancel out, and

$$\exp(i\phi_n - i\phi_m) \equiv \cos(\phi_n - \phi_m), \tag{3.20}$$

under the sum.

Also, the ensemble mean cancels the second summation because $\langle \exp(i\phi_n - i\phi_m)\rangle = \delta_{n,m}$, and the term $n = m$ is not in the sum. Because of that,

$$\langle \mathcal{E}^*(x)\mathcal{E}(x)\rangle = \sum_{n=0}^{\infty} |a_n|^2 |\psi_n(x)|^2 = I(x). \tag{3.21}$$

For the product

$$|\mathcal{E}(x)|^2|\mathcal{E}(y)|^2 = I(x)I(y) + \sum_{\substack{m,n,p=0 \\ m\neq n}}^{\infty} a_m^* a_n |a_p|^2 \psi_m^*(x)\psi_n(x)|\psi_p(y)|^2 +$$

$$\sum_{\substack{m,n,p=0 \\ m\neq n}}^{\infty} a_m^* a_n |a_p|^2 \psi_m^*(y)\psi_n(y)|\psi_p(x)|^2 + \sum_{\substack{m,n,p,q=0 \\ m\neq n, p\neq q}}^{\infty} a_m^* a_n a_p^* a_q \psi_m^*(x)\psi_n(x)\psi_p^*(y)\psi_q(y), \tag{3.22}$$

the terms involving $a_m^* a_n$ are not relevant here, because their ensemble average will return 0. For the term with $a_m^* a_n a_p^* a_q$, the average goes as

$$\left\langle a_m^* a_n a_p^* a_q \right\rangle \propto \langle \exp i(\phi_n - \phi_m + \phi_q - \phi_p)\rangle = \delta_{n,m}\delta_{q,p} + \delta_{n,p}\delta_{m,q}. \tag{3.23}$$

The first of these Kronecker deltas is not contained in the sum and can be ignored. This allows the last summation in Equation (3.22) to be written as

$$\sum_{\substack{m,n=0 \\ m\neq n}}^{\infty} |a_m|^2 |a_n|^2 \psi_m^*(x)\psi_m(y)\psi_n^*(y)\psi_n(x). \tag{3.24}$$

The sum can then be reordered as,

$$\sum_{n=0}^{\infty} |a_n|^2 \psi_n^*(y)\psi_n(x) \left[\sum_{\substack{m=0 \\ m\neq n}}^{\infty} |a_m|^2 \psi_m^*(x)\psi_m(y) \right], \tag{3.25}$$

where the sum over m should be performed first. The constraint $m \neq n$ can now be removed by subtracting $|a_n|^2\psi_n^*(x)\psi_n(y)$ from the square brackets.

Since $W(x,y) = \sum_{m=0}^{\infty} |a_m|^2 \psi_m^*(x)\psi_m(y)$, the term in Equation (3.25) becomes

$$\sum_{n=0}^{\infty} |a_n|^2 \psi_n^*(y)\psi_n(x) \left[W(x,y) - |a_n|^2 \psi_n^*(x)\psi_n(y) \right]. \tag{3.26}$$

Finally, it is possible to write $\langle |\mathcal{E}(x)|^2 |\mathcal{E}(y)|^2 \rangle = R(x,y)$ as,

$$R(x_1,x_2) = \langle \mathcal{E}^*(x_1)\mathcal{E}(x_1)\, \mathcal{E}^*(x_2)\mathcal{E}(x_2) \rangle \tag{3.27}$$

$$= I(x_1)I(x_2) + |W(x_1,x_2)|^2 - C(x_1,x_2), \tag{3.28}$$

and

$$C(x_1,x_2) = \sum_{n=0}^{\infty} |a_n|^4 |\psi_n(x_1)|^2 |\psi_n(x_2)|^2. \tag{3.29}$$

In the limit $M_x^2 \gg 1$,

$$C(x_1,x_2) = \frac{4}{T_x^2} \sum_{n=0}^{\infty} |\psi_n(x_1)|^2 |\psi_n(x_2)|^2 \to 0. \tag{3.30}$$

Since $C(x_1,x_2) \approx 0$, the intensity statistics are well defined in terms of the CSD in the large temperature limit.

$C(x_1,x_2)$ arises in Equation (3.28) from the ensemble averages over phase differences. Therefore $C(x_1,x_2)$ can be easily overlooked because it only becomes significant in the limit of 2 to 3 modes. Also, since $C(x_1,x_2)$ contains mode amplitudes raised to the fourth power if there is a mode j which $|a_j|^2 \approx 1$ then $|a_j|^4 \approx 1$ and $C(x_1,x_2) \gg 0$.

Now, if $|a_n|^2 \ll 1$ for all modes, then $|a_n|^4$ will be even smaller and $R(x_1,x_2)$ from Equation (3.29) becomes negligible. Particularly, for a beam with a poor quality factor such as $M_x^2 > 19$, $C(x_1,x_2)$ is negligible because the largest mode amplitude $|a_0|^2 = 2/(M_x^2+1) < 0.1$.

However, the description presented in this section does not describe well the coherence state of a beam with only a few relevant modes. Because, for a single occupied mode j, Equation (3.25) is approximately zero. As $|a_j|^2$ always appears multiplied by $|a_{m\neq j}|^2 \approx 0$, such that

$$R(x,y) \approx I(x)I(y). \tag{3.31}$$

Since Equation (3.31) describes a thermodynamic beam in the few modes limit, the statistical information available does not identify any signatures of the beam coherence state. The statistical content of the beam is encoded in M_x^2, which is not present in Equation (3.13).

This can be observed in Figure 6. The contributions of each parameter in the expression describing $R(x_1, x_2)$ (Equation (3.28)) can be analyzed. The contributions due to C (solid lines) have longer tails than those due to $|W|^2$ (dashed lines). This distinction is particularly clear when $M_x^2 \geq 1.41$. And even more expressively, $M_x^2 \approx 1$, both curves are essentially identical. The information about M_x^2 is located where the field amplitude is very small. Also, $|W|^2$ and $-C$ cancel each other in this limit, making it very difficult to distinguish M_x^2 and retrieve the associated temperature.

Figure 6 – Each term of Equation (3.28) is plotted. $\int |W(x, x+\Delta x)|^2\, dx$ (dashed red lines) and $\int C(x, x+\Delta x)\, dx$ (solid blue lines) are shown as functions of Δx (horizontal axis). The ensemble means $I(x)$ is also plotted for reference (yellow-filled region). Each term in Equation (3.28) has a spatial correlation that depends on M_x^2. For small M_x^2, the distance between the dashed and solid lines implies that the intensity autocorrelation is inappropriate to measure M_x^2.

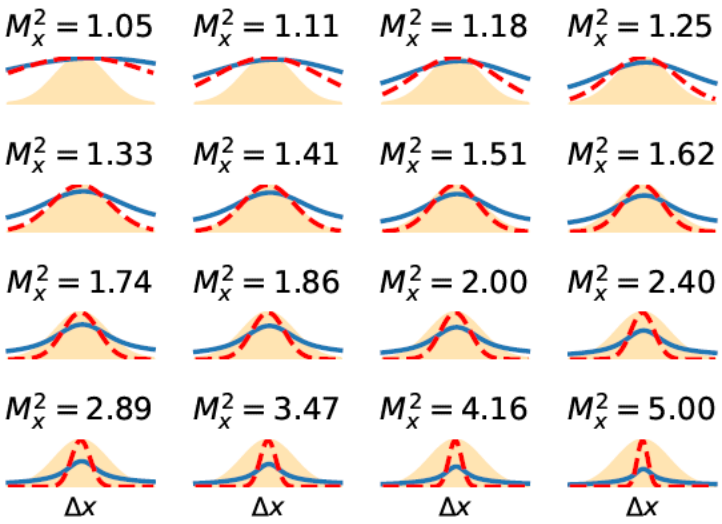

Source: Author (2024)

3.2 STATISTICAL ANALYSIS OF ENSEMBLES WITH A FIXED M_x^2

To properly analyze statistically the wavefront of a beam, even in the limit of few modes ($M_x^2 \approx 1$), the deviations from the ensemble average behavior are used to enhance the response associated with M_x^2, utilizing concepts from photonic glassy systems (PIERANGELI et al., 2017).

The thermodynamic beam described in Section 2.3.2 has a fixed M_x^2 and W_x^2. Suppose that such a beam can be fabricated α-times, with $\alpha(= 1, 2, \dots)$. From Equation (2.24), the

field state α can be written as,

$$\mathcal{E}_\alpha(x) = \sum_{n=0}^{\infty} a_n^\alpha \psi_n(x). \tag{3.32}$$

For each state α the coefficients $a_n^\alpha = |a_n| e^{i\phi_n^\alpha}$ are distinguished from each other by their particular set of phases ϕ_n^α, which remain fixed during the state measurement. Also, the phases of distinct states α and β are statistically independent, while for a given M_x^2 the mode amplitude $|a_n|$ remains constant over different states, as can be seen in Equation (2.61).

The intensity profile for the state α is

$$I_\alpha(x) = \mathcal{E}_\alpha^*(x)\mathcal{E}_\alpha(x) = I(x) + \sum_{\substack{m,n=0 \\ m\neq n}}^{\infty} a_m^{\alpha *} a_n^\alpha \psi_m^*(x)\psi_n(x), \tag{3.33}$$

where $I(x)$ corresponds to the ensemble average of the intensity profile. However, the double sum in Equation (3.33) depends on the mode state phases, and so the fluctuations regarding the ensemble average,

$$\Delta_\alpha(x) = I_\alpha(x) - I(x), \tag{3.34}$$

carry information about the interference among modes in the state α.

Additionally, since $\langle \Delta_\alpha(x) \rangle = 0$, the comparison of the sum in Equation (3.33) with Equation (3.22) leads to the average correlation between fluctuations regarding points x_1 and x_2 in the same state α, which is given by

$$\langle \Delta_\alpha(x_1)\Delta_\alpha(x_2) \rangle = |W(x_1, x_2)|^2 - C(x_1, x_2). \tag{3.35}$$

The analysis of the wavefront states allows the retrieval of different information than that on Equation (3.35), which is particularly useful for small M_x^2 values since the description requires only a few coherent modes. Specifically, the Pearson correlation coefficient between distinct states, α and β,

$$r_{\alpha\beta} = \frac{\int \Delta_\alpha(x)\Delta_\beta(x)dx}{\sqrt{\int [\Delta_\alpha(x)]^2\, dx}\sqrt{\int [\Delta_\beta(x)]^2\, dx}}, \tag{3.36}$$

measures the correlation between fluctuations associated with the wavefronts α and β across x. The parameter $r_{\alpha\beta}$ is normalized such that $-1 \leq r_{\alpha\beta} \leq 1$, and the consideration of all distinct pairs of states creates a distribution $P(r)$ of $r_{\alpha\beta}$-values. The Pearson correlation coefficient is introduced here as a complementary way of retrieving the coherence state of an ensemble, particularly in the case of nearly coherent beams.

Some particular cases are explicitly analyzed to better understand the information obtained from the distribution $P(r)$.

1. If the beam has just a single mode, $I_\alpha(x) = I(x)$ for all states, then $\Delta^{(\alpha)}(x) = 0$ and only $r_{\alpha\beta} = 0$ will be observed. This means that $P(r)$ is a Dirac delta distribution.

2. If $\Delta_\alpha(x)$ varies completely randomly fashion, there is a large number of occupied modes, then the central limit theorem indicates that the sum associated with $\Delta_\alpha(x)\Delta_\beta(x)$ is statistically described by a Gaussian distribution centered at zero.

3. If $\Delta_\alpha(x)$ and $\Delta_\beta(x)$ are strongly (anti-) correlated, so that the extreme value $(r_{\alpha\beta} = -1)\, r_{\alpha\beta} = 1$ is reached. This represents a system approximated by two modes because for the state $\mathcal{E}_\alpha(x) = a_0\psi_0(x) + a_1\psi_1(x)$, the phase variation $\Delta\phi_\alpha = \phi_1^\alpha - \phi_0^\alpha$ and mode $\psi_n(x)$ real, allows Equation (3.36) to be written as

$$r_{\alpha\beta}^{(\text{2 modes})} = \frac{\cos\Delta\phi_\alpha}{|\cos\Delta\phi_\alpha|}\frac{\cos\Delta\phi_\beta}{|\cos\Delta\phi_\beta|} = \pm 1. \tag{3.37}$$

To explicitly show the nuances of such a distribution, eight α states are analyzed through the ratio $I_\alpha(x)/I(x)$ (PIERANGELI et al., 2017), Figure 7.

Figure 7 – The intensity profile $I_\alpha(x)$ (solid colored lines), normalized by the average intensity $I(x)$ (black dashed lines) is plotted as a function of the normalized distance $\frac{x}{W_x}$ for various M_x^2 values. Each colored solid line represents one of the possible state alpha for a fixed M_x^2. In the few modes regime ($M_x^2 = 1.05$), two groups of lines can be observed, which leads in Equation (3.36) to a fully correlated $(r_{\alpha\beta} = +1)$ or anticorrelated $(r_{\alpha\beta} = -1)$ states. As the number of modes increases, so does the M_x^2 value. This also increases the randomness, leading to a reduction of the absolute values of $r_{\alpha\beta}$.

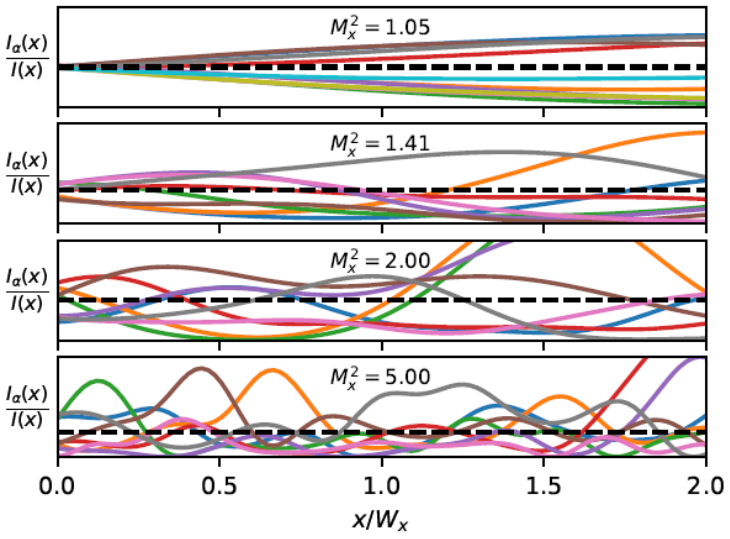

Source: Author (2024)

The dashed horizontal lines in Figure 7 show the average intensity $I(x)$, from which the fluctuations $\Delta_\alpha(x)$ can be inferred as a function of x (Equation (3.34)). In the few modes

or low-temperature regime ($M_x^2 = 1.05$) two separate groups of lines remain well defined for the whole range of x. In this situation, if states α and β belong to the same group, then $\Delta_\alpha(x)\Delta_\beta(x) > 0$ for all x, from Equation (3.36) the maximum value $r_{\alpha\beta} = +1$ (full correlation). However if α and β belong to different groups, then $\Delta_\alpha(x)\Delta_\beta(x) < 0$ for all x and $r_{\alpha\beta} = -1$ (full anticorrelation). Physically this means that the beam wanders around $x = 0$.

When more modes are added, implying higher M_x^2 (and T_x) values, the randomness of $\Delta_\alpha(x)\Delta_\beta(x)$ around $I(x)$ also increases. Which leads to fluctuations in $\Delta_\alpha(x)\Delta_\beta(x)$ and $r_{\alpha\beta}$ to decrease in absolute value.

This section focused on utilizing the Pearson correlation parameter Equation (3.36) to obtain a distribution $P(r)$. This distribution encodes statistical information regarding the state of coherence of a beam, from regimes of few to a large number of available spatial modes. All of this information can be retrieved only with snapshots of the beam wavefront. The different $P(r)$ distributions obtained can be theoretically predicted through the central limit theorem. The following section shows how the distribution profiles can be predicted, utilizing only statistical arguments.

3.3 PREDICTION OF ENSEMBLES DISTRIBUTIONS THROUGH FISHER TRANSFORM

The distribution $P(r)$ can be approximately predicted by noticing from the central limit theorem that it should converge to a Gaussian as the number of terms increases in the sum in x in Equation (3.36). The convergence rate depends on the details of the distributions for $\Delta_\alpha(x)$ and $\Delta_\beta(x)$, but it has been previously shown that the Fisher transform (HOTELLING, 2018),

$$z_{\alpha\beta} = arctanh\left(r_{\alpha\beta}\right) \tag{3.38}$$

accelerates this convergence. Since $z_{\alpha\beta}$ is Gaussian distributed, with mean μ and variance σ^2, the inverse Fisher transform can be taken to obtain the distribution (RAPOSO et al., 2019),

$$P(r) = \frac{1}{\sqrt{2\pi\sigma^2}} \frac{1}{1-r^2} \exp\left\{-\frac{\left[arctanh\left(r\right) - \mu\right]^2}{2\sigma^2}\right\}. \tag{3.39}$$

The characteristics of interest of the distribution Equation (3.39) are shown in Figure 8. When the variance of the correlations is large, $P(r)$ is strongly peaked around $r = \pm 1$, as expected for the thermodynamic beam in the few modes regime (low M_x^2 and T_x). A decrease in σ leads to a zero-centered Gaussian distribution, consistent with the many modes

regime (high M_x^2 and T_x). In this way, Equation (3.39) approximates the behavior of the $r_{\alpha\beta}$ distribution for all M_x^2 values.

Figure 8 – The normalized $P(r)$ distribution in Equation (3.39) is plotted as a function of r, $(-1 \leq r \leq 1)$. Here $\mu = 0$ for all samples.

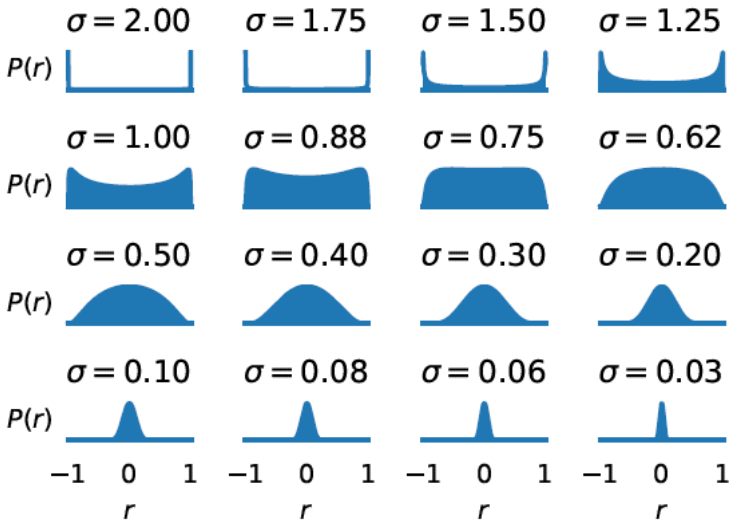

Source: Author (2024)

Finally, some numerical simulations of Equation (3.36) have been made with the thermodynamic beam for different values of M_x^2. The obtained $P(r)$ were then fitted with the distribution from Equation (3.39). Some observations can be made from it:

1. The mean $\mu \approx 0$ was obtained for the whole range $M_x^2 \in [1.01, 5.00]$, while the best-fit values for σ are shown in the blue line in Figure 9.

2. There is an approximate dependence $\sigma \approx \frac{1}{M_x^2}$ for $M_x^2 > 1.4$, in this situation the mode temperature can be readily estimated for beams effectively containing more than two modes. A finer analysis of the large-M_x^2 asymptotic behavior data indicates that $\sigma \approx (1/M_x^2)^{1.06}$ describes more closely the relation between σ and M_x^2 in this regime. While in the limit of only two modes, the distribution $P(r)$ becomes strongly peaked at the side extremes $r = \pm 1$ (Equation (3.37)). This case is far from the large-M_x^2 asymptotic behavior in Figure 9. However, the product $M_x^2\sigma$ increases fast when $M_x^2 \to 1$, so that the empirical function with a low-M_x^2 correction to the behavior $(1/M_x^2)^{1.06}$,

$$f(M_x^2) = \frac{1}{(M_x^2)^{1.06}} \left(0.06 T_x^{-2.3} + 1\right), \tag{3.40}$$

matches the data of σ in both $M_x^2 \to 1$, and large M_x^2 limits, as can be seen in Figure 9. In Equation (3.40), the dependence of the temperature T_x on M_x^2 is given by Equation (2.60).

Figure 9 – The parameter σ (solid blue line) from fitting Equation (3.39) to numerical data of $P(r)$ as a function of M_x^2. The dashed green line shows the approximate asymptotic behavior for M_x^2 1.4. The orange dots represent the empirical expression for σ in Equation (3.40), with a good match in both $M_x^2 \to 1$ (inset) and large-M_x^2 limits.

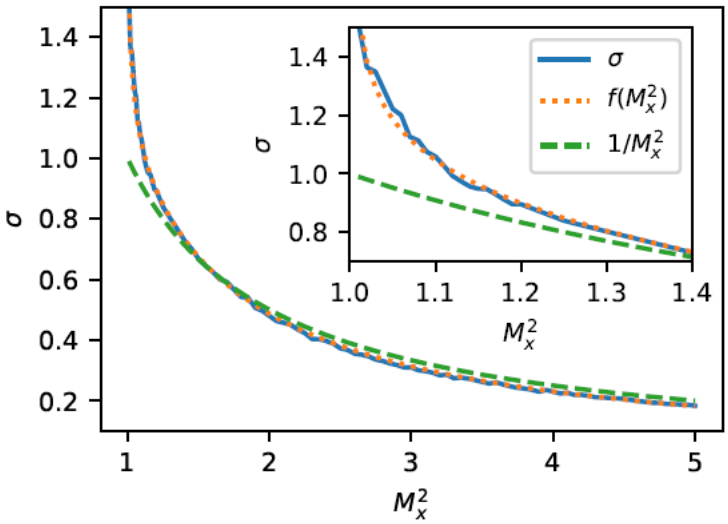

Source: Author (2024)

4 HOLOGRAPHY

To generate the thermodynamic beam experimentally holography will be used. The following chapter introduces the key concepts that allow for the experimental realization of such a beam. that Holography allows to reproduce the electromagnetic field across the entire space due to an illuminated object without needing the original object (Figure 10). The desired effect is produced by a hologram which modulates the incident light beam with adequate amplitude and phase patterns. There are different approaches to produce holograms, such as holographic films or phase masks. The hologram is responsible for storing the amplitude and phase information of the electromagnetic field associated with the interference pattern between the reference wave and the wave from the objects.

Figure 10 – Holography consists of two steps. Hologram recording (a), which records the wavefront of an arbitrary object interfering with a reference wave. The object reconstruction (b) retrieves the wavefront associated with the original objects without the need for the original object. This two-step process is a characteristic of off-axis holography.

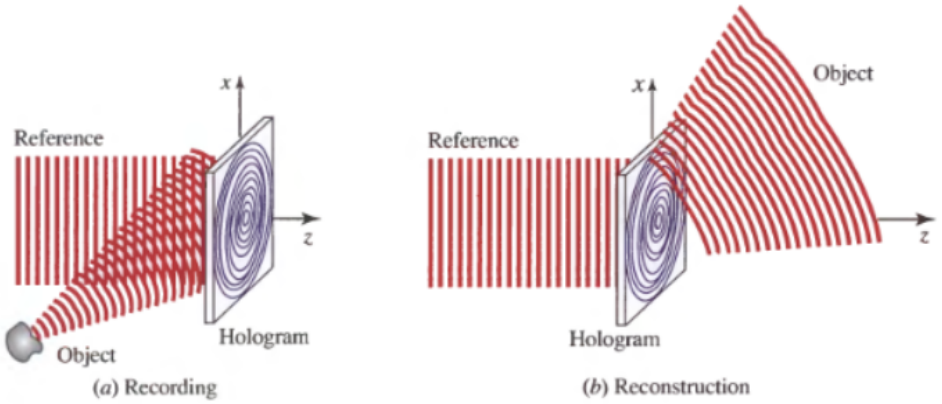

Source: SALEH; TEICH (2019)

Instead of using holographic films, this work generates holograms through digitally designed phase masks applied on a Spatial Light Modulator (SLM). The fundamentals of SLM will be discussed shortly, but in essence, they allow to spatially control the phase of the optical fields. More specifically, off-axis holography is employed to ensure that the wave used to illuminate the hologram, or reference wave, and the generated wave propagate along different directions and can be more easily separated using a spatial filter. This chapter shows the principal concepts of holography that will be used in this work to generate structured light. Later, these ideas will be used to generate beams with thermodynamical properties, here called thermodynamic beams.

4.1 SPATIAL LIGHT MODULATORS

A SLM is a digital device that shapes either the amplitude or phase of light with computer-generated holograms (Figure 11). The hologram containing the desired amplitude or phase information is uploaded to the SLM screen, which in turn gives the desired properties to the light beam through the arranging of the pixels. In this work, we have used phase-only SLMs, which operate through the birefringence of liquid crystal molecules. A schematic of a single pixel is shown in Figure 11.

Figure 11 – Schematic representation of a SLM.

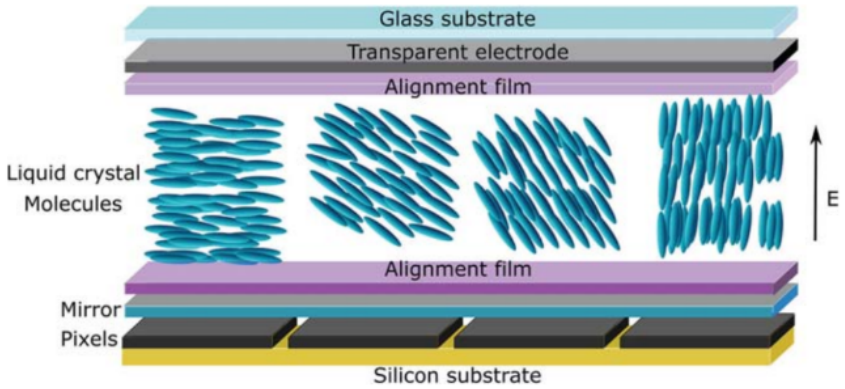

Source: ROSALES-GUZMÁN; FORBES (2017)

The liquid crystal has an anisotropic refractive index that allows the modulation of light beams with molecular reorientation. Its molecules still have an organized crystal lattice, however since it is liquid, it allows some flexibility in the alignment of the molecules. For instance, without an applied external field E, all molecules are arranged horizontally in Figure 11.

Since the binding forces of the molecule are stronger in specific crystalline directions, the liquid crystal is a birefringent material. For neumatic liquid crystals, as shown in Figure 11, there is a molecular dipole along the axis of the molecule and a different dipole momentum in the other two transversal directions. Suppose that the incident wave is horizontally polarized in Figure 11, for $E = 0$ the refractive index is higher than when E is maximum and all the molecules are vertically oriented. The susceptibility and polarization are proportional to the dipole momentum associated with the coupling between the light and the media. Along the long axis, the refractive index is n_e, while for the transverse axes, the associated refractive index is n_o. This allows the phase introduction to the reference wave.

The SLM has millions of pixels filled with liquid crystal molecules. A computer can indi-

vidually control these pixels, allowing a fine modulation of the desired light beam. How these pixels are controlled is determined by two internal parameters of the SLM: the internal potentiometers and the gamma curve, which determine how the liquid crystal molecules are rotated and the desired phases added to the reference wave. More specifically, the potentiometer values are associated with the minimum and maximum electric fields used to orient the liquid crystal molecules, while the gamma curve compensates for the nonlinearity of the molecule orientation dynamics (LI; CAO, 2019).

The applied voltage controls how the liquid crystal molecules rotate, generating the phase shifts in the light beam. As the applied voltage changes, so does the rotation angle of the liquid crystal molecules with respect to the horizontal (or electrodes) plane. Effectively, the SLM works as a phase retarder for the electric fields component along the plane of Figure 11, generating a phase variation of $\Delta\delta$, given by

$$\Delta\delta = \frac{2\pi}{\lambda}(n_e - n_o)d, \tag{4.1}$$

where n_o and n_e are the ordinary and extraordinary index of refraction, respectively, d is the thickness of the liquid crystal, and λ is the wavelength of the light beam. The extraordinary index n_e depends on the voltages applied by the SLM driver circuit, more details are discussed in (ROSALES-GUZMÁN; FORBES, 2017) and (LI; CAO, 2019).

The internal potentiometer and the gamma curve configure how the SLM gives the phase shift to the light beam. The SLM modulation works in grayscale in an 8-bit scale ranging from 0 to 255. Ideally for our applications the phase shifts should go from 0 (black, or a gray level of 0) to 2π (white, or a gray level of 255) and vary linearly for all values in between. To give this kind of modulation to the SLM it is necessary to find the correct values of potentiometers and the correct gamma curve. Usually, the SLM's manual provides the basic configurations to have this kind of modulation. However, due to variations in wavelength, age, humidity, and many other factors, this basic configuration often is ineffective in obtaining the desired modulation, and it is important to calibrate the SLM properly.

4.1.1 Signals of trouble with Spatial Light Modulators

A good indication that the SLM is doing the phase modulation it should, can be inferred by a simple analysis with a powermeter (Figure 12). The basic principle in the following analysis is that the SLM only modulates one component of the incident beam polarization.

Figure 12 – Experimental setup to measure possible errs on the SLM calibration. $\lambda/2$ is a half waveplate, PBS is a polarizer beam splitter and $\lambda/4$ is a quarter waveplate.

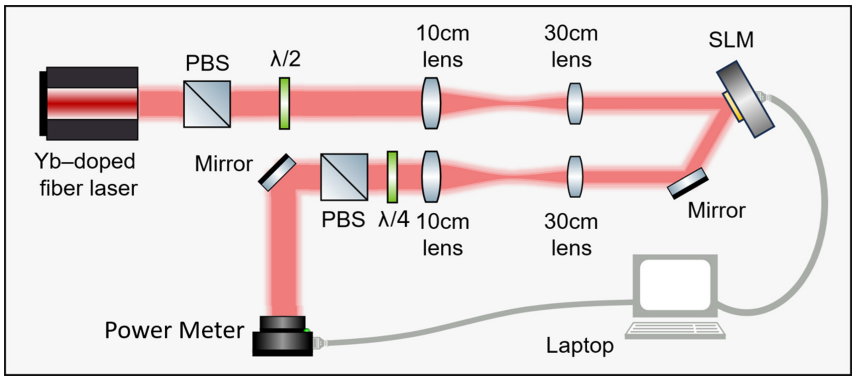

Source: Author (2024)

The procedure goes as follows:

1. The quarter wave plate is set at 0^{o}. The output is maximized with the half waveplate.

2. The output is adjusted at half the maximum with the half waveplate and the quarter waveplate goes to 45^{o}.

3. A constant phase is applied at the SLM, and a sweep is performed. In steps of 1^{o}, the constant phase goes from 0 to 2π and the power is collected at the powermeter.

When the sweep is completed, the power as a function of the applied phase is obtained (Figure 13(b)). If the SLM is calibrated the expected curve should be sinusoidal (13(a)). For the SLM used in this work (Figure 13(b)), not only there was a discontinuity, but the sinusoidal curve was distorted, which points to the need for a calibration.

Figure 13 – (a) Expected phase modulation of a calibrated SLM. (b) Measured phase modulation for the SLM used in this work.

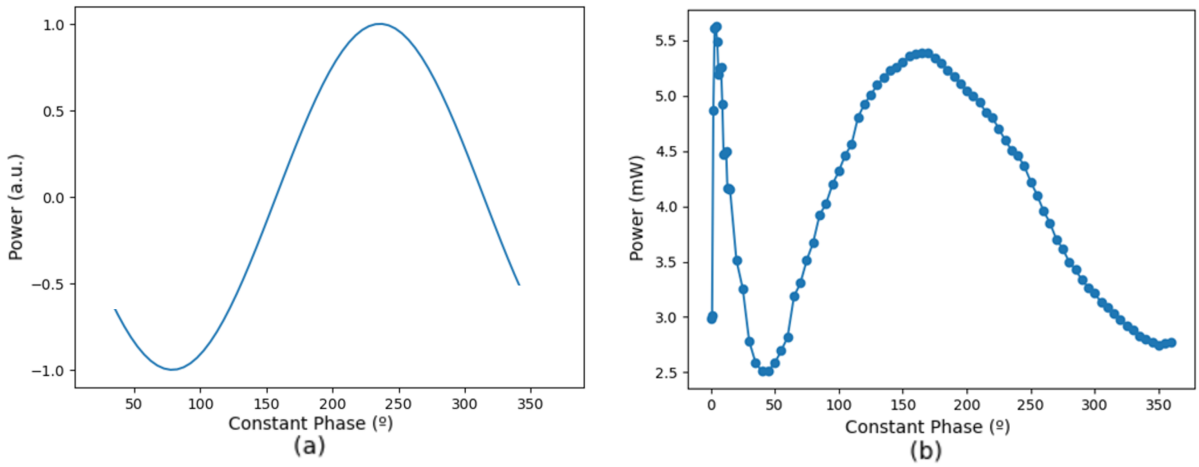

Source: Author (2024)

4.1.2 Calibration of Spatial Light Modulators

To get the correct calibration for the SLM, the internal potentiometers and gamma curve need to be both checked and correctly set (Figure 14). The values of the internal potentiometers and the shape of the gamma curve can be changed at the software that comes with the SLM.

Figure 14 – Internal Potentiometers (a) and Gamma Curve (b) as presented on the SLM software.

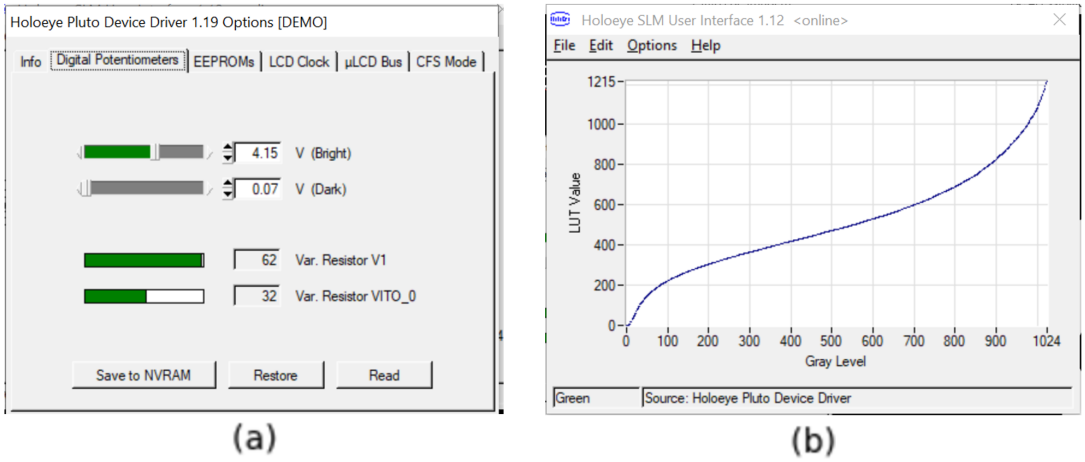

Source: Author (2024)

The Interferometric Phase Calibration Method (IPCM) was used to measure and correctly calibrate the SLM (LI; CAO, 2019). A double slit is generated at the SLM screen, and a lens allows the observation of the interference pattern at a camera (Figure 15). As the relative phase between each beam varies according to the gray level, the position of the bright and dark fringes of the interference pattern also changes. To obtain the total phase shift implemented by the SLM, one needs only to track the changes in the position of the fringes according to the gray level and then convert these values back to phase.

The IPCM allows the reconstruction of both phase and amplitude by mathematical methods since the phase shift and intensity profiles of the beams are directly related by

$$I(x,y) = I_r(x,y) + I_v(x,y) + 2\sqrt{I_r(x,y)I_v(x,y)}cos(\delta), \tag{4.2}$$

where $I(x,y)$ is the interference fringes, $I_r(x,y)$ and $I_v(x,y)$ are the intensity distributions of the constant or reference beam and the varying beam, respectively, and δ is the phase difference between the beams.

This means that this method requires only recording the intensity profile of the interference pattern created by the beam with a fixed constant phase mask and the same beam with a

Figure 15 – Experimental setup for SLM calibration. PS is the light source, L1 and L2 are lenses, MASK is a double slit aperture, P is a polarizer and, CAM is a camera.

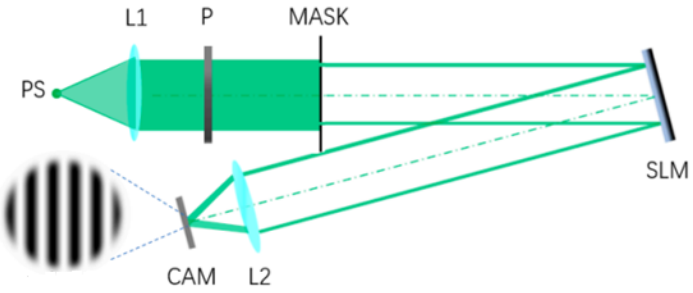

Source: LI; CAO (2019)

varying constant phase mask. The mask applied and a typical interference pattern obtained can be seen in Figure 16.

Figure 16 – The applied mask consists of the superposition of a phase constant mask (a) and a diffraction grating (b). The diffraction grating is applied to calibrate the SLM in the closest condition to the experimental setup. Since all complex masks used in this work require a diffraction grating to be generated, the calibration is conducted as such. (c) Corresponds to the generated interference pattern by such a mask.

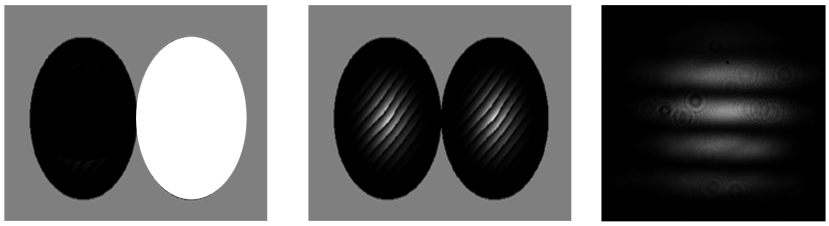

Source: Author (2024)

In this work, the gray level on the varying beam went from 0 to 255 in steps of 5. Once these patterns were recorded as images with a camera, to obtain the total phase shift, firstly the minima of intensity are found in each image. Then the position of the minima is tracked in all images and analyzed as a function of the phase variation applied at the varying beam. With this analysis, it is possible to retrieve the experimental total phase shift applied by the SLM. If the phase shift is far from 2π, then the internal potentiometers need to be adjusted. If the phase does not vary linearly in the interval from 0 to 2π, then the gamma curve needs to be corrected. Since the phase shift is already tracked, and the goal is a linear variation, after finding good values for the potentiometers, one needs only a new gamma curve to correct the modulation nonlinearity.

With the IPCM, the basic configurations of the SLM used in this work, as the manual

suggests, were applied. They are a linear gamma curve and internal potentiometers at 4.19V (Dark) and 0.03V (Bright). Two principal characteristics were expected and wanted: as the phase masks vary the total phase shift is 2π, and the phase variation occurs linearly from black (0) to white (2π). However, the data from Figure 13 already indicates that not only the phase shift was wrong, but the modulation response was not linear. This means that both the gamma curve and internal potentiometers should be calibrated.

The parameters need to be separately corrected. The potentiometers require a trial-and-error approach. Several values were tried at first, and randomly chosen. After passing the collected images of the 0 to 2π swept through the IPCM and receiving the experimental total phase shift, the potentiometer values for approximate 2π phase modulation were found. To the SLM and wavelength used in this work, the potentiometer values that correspond to a total phase modulation of 2π are 2.08 V (Dark) and 0.96 V (Bright). After determining the correct total phase shift, the correct gamma curve can be obtained through the IPCM, once the program tracks the fringes in the collected images, it notices the problems in the modulation and creates a gamma curve that gives the desired linear modulation. For the SLM used in this work, the desired gamma curve can be seen in Figure 17.

Figure 17 – (a) Gamma curve that gives a linear modulation to the SLM used in this work. (b) Linear modulation obtained calibrated gamma curve, the orange line corresponds to a linear function, while the blue line is the new gamma curve.

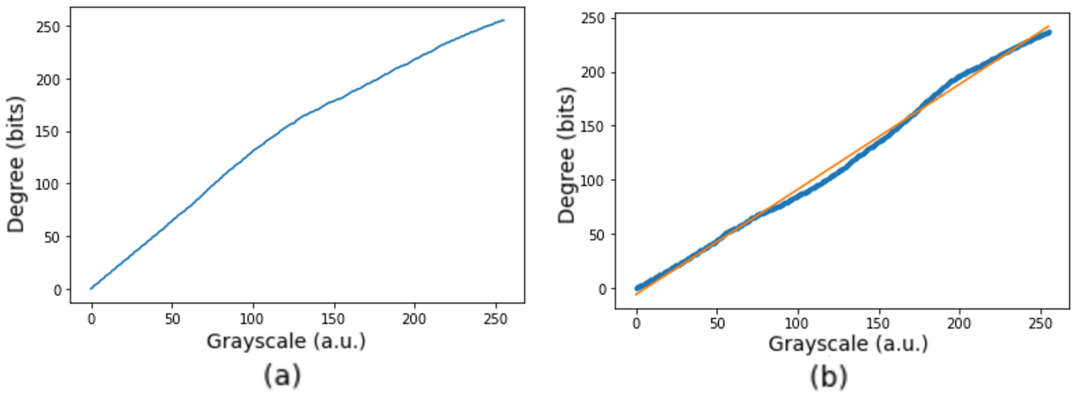

Source: Author (2024)

4.2 OFF-AXIS HOLOGRAPHY

Holography can be analyzed through the angle between the propagation axes of the reference wave and the output beam, which contains the desired phase pattern. When the desired

beam is parallel to the reference beam, it is called in-line holography. Off-axis holography happens when the reference beam forms an angle, θ_{ref}, with the output beam. Both cases are shown in Figure 18.

Figure 18 – Difference between in-line and off-axis holography.

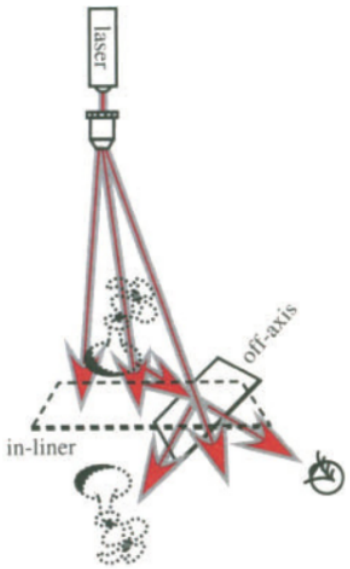

Source: BENTON; BOVE (2008)

The biggest characteristic of off-axis holography, which is particularly useful when using SLMs, is having the output and reference beam well separated in space (Figure 19). Which simplifies the retrieval of the beam with the desired modulation. The spatial filter needed to separate the desired beam is more easily and efficiently implemented. In this work, only one iris is needed to clear out all the other diffraction orders and retrieve the first diffraction order, which contains the desired modulation.

The following discussion is heavily based on (BENTON; BOVE, 2008) and shows the general behavior of off-axis holography, that will later on be used to generate structured light.

Here we are interested in analyzing how the characteristics of the reference and object beam interfere with the output beam. The reference beam interferes with the object beam, creating the mask. Once the mask is illuminated with the reference beam, the effect the object has on the reference beam is reproduced. The object can be understood here as some arbitrary component that gives a specific phase change to the reference beam that we are interested in recording and reproducing. For the discussion proposed here, the beam that later illuminates the hologram is the same as the reference beam, which is used to record the hologram.

To start the discussion, it is defined that the reference beam forms an angle, θ_{ref}, and

Figure 19 – Schematic description of the angle between the reference and object beams utilized in off-axis holography.

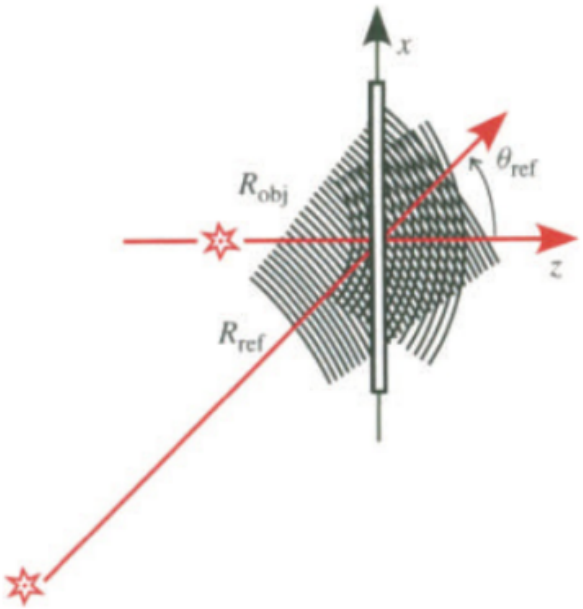

Source: BENTON; BOVE (2008)

the object beam is on-axis (Figure 19). The phase of the reference beam, which is an off-axis spherical wave is

$$\Phi_{ref}(x,y) = \Phi_{obj,0} + \frac{2\pi}{\lambda} sin(\theta_{ref})x + \frac{\pi}{\lambda}\left[\frac{cos^2(\theta_{ref})}{R_{ref}}x^2 + \frac{1}{R_{ref}}y^2\right], \tag{4.3}$$

where λ is the beam wavelength and R_{ref} is the curvature of the reference beam.

The phase of the object beam, which is an on-axis ($\theta_{ref} = 0$) object is given by

$$\Phi_{obj}(x,y) = \Phi_{obj,0} + \frac{\pi}{\lambda R_{obj}}(x^2 + y^2). \tag{4.4}$$

And finally, the output beam is

$$\Phi_{out,m}(x,y) = m\left[\Phi_{obj}(x,y) - \Phi_{ref}(x,y)\right] + \Phi_{ref}(x,y), \tag{4.5}$$

where m indicates the order of diffraction of the output beam. Equation (4.5) describes how the output beam behaves as a function of the reference and object beam. When $m = 0$, the reference beam is retrieved, as expected to the zeroth order of diffraction. For $m = 1$, the object beam is fully retrieved, which is the desired result. The appearance of diffraction orders comes from the interference pattern generated by the reference and object waves. (BENTON; BOVE, 2008) offers a detailed description.

The output beam can be written as,

$$\Phi_{out,m}(x,y) = \Phi_{out,0} + \frac{2\pi}{\lambda} sin(\theta_{out})x + \frac{\pi}{\lambda}\left[\frac{cos^2(\theta_{ref})}{R_{ref}}x^2 + \frac{1}{R_{ref}}y^2\right]. \tag{4.6}$$

Then, the coefficients of the terms for x, x^2, and y^2 are matched for the three beams. The following expressions are obtained,

$$sin(\theta_{out,m}) = -msin(\theta_{ref}), \tag{4.7}$$

$$\frac{cos^2(\theta_{out,m})}{R_{out,m,x}} = m\left[\frac{1}{R_{obj}} - \frac{cos^2(\theta_{ref})}{R_{ref}}\right] + \frac{cos^2(\theta_{ref})}{R_{ref}}, \tag{4.8}$$

$$\frac{1}{R_{out,m,y}} = m\left(\frac{1}{R_{obj}} - \frac{1}{R_{ref}}\right) + \frac{1}{R_{ref}}. \tag{4.9}$$

Which describes how the output beam behaves in off-axis holography. The previously presented description is valid for transmission holograms, however, reflection holograms are also employed. The physics principles behind both cases are the same, and Equations 4.7, 4.8, and 4.9 can be easily transformed by $\theta_{transmission} = sin(\theta_{reflection})$.

5 EXPERIMENTAL GENERATION OF THERMODYNAMICAL BEAMS AND COHERENCE ANALYSIS

With the thermodynamic description for light propagating in free-space light, based on analysis of the beam wavefront developed in Chapters 2 and 3. This chapter now focuses on the generation of the thermodynamic beams experimentally and further statistical analysis.

5.1 EXPERIMENTAL SETUP AND ITS CHARACTERIZATION

To generate a thermodynamic beam an SLM, (pixel size 8.0 μm; 1920$\times$1080 resolution), (ARRIZÓN et al., 2007), (BOLDUC et al., 2013), is employed. The experimental setup can be seen in Figure 20. The light source used was a homemade mode-locked Ytterbium single-mode fiber laser (1030 nm, 140 fs @ 130 MHz, 70 mW), further described in Reference (MÉLO et al., 2018). The pair, half waveplate ($\frac{\lambda}{2}$) and Polarizing Beam Splitter (PBS), are used for power control. The output beam has an approximate diameter of 1 mm, and a telescope is used to expand the beam and illuminate the SLM. Then, the beam is contracted to its original size. Since off-axis holography (Section 4.2) is used to generate the phase masks applied to the SLM, a mirror and an iris to filter the first diffracted order is all that is needed to pick up the beam with the desired phase modulation. A lens is used to focalize the beam into a Charged Coupled Device (CCD) (pixel size 4.65 μm; 1024x768 resolution). It is important to point out that better measurement resolution is achieved when the beam illuminates as much of the CCD sensor as possible.

Figure 20 – Experimental setup. $\lambda/2$ is a half waveplate, PBS is a Polarizing Beam Splitter, and CCD is a Coupled Charged Device.

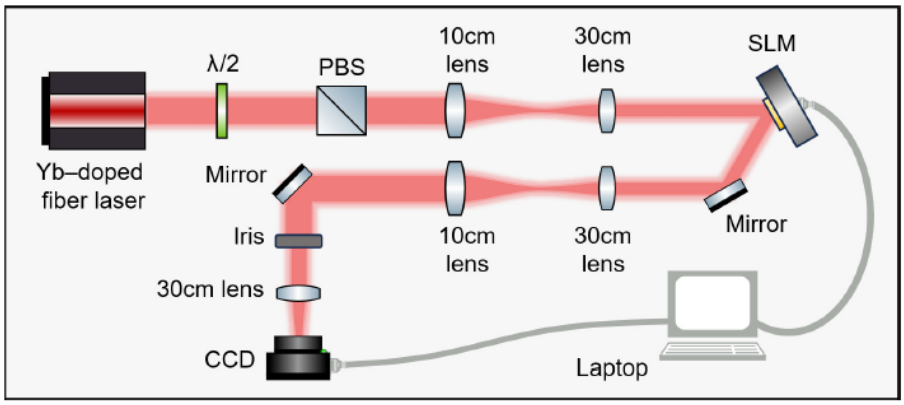

Source: Author (2024)

Before any measurements, it is important to guarantee that the setup works as intended. First, the modulation generated by the SLM is tested. In Figure 21 (a) a Gaussian beam is generated by the SLM and in (b) a beam with orbital angular momentum m=1 is generated and used to check the modulation, as well as to make sure that the masks are being applied to the center of the beam. Which can be inferred from the vortex being in the center of the beam.

Figure 21 – Modulation test for the SLM. A Gaussian beam (a) and a beam with angular momentum m=1 (b) is generated by the SLM.

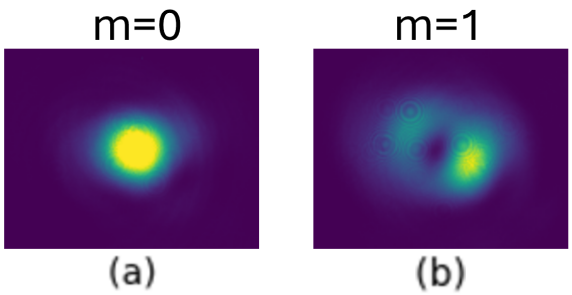

Source: Author (2024)

Another important characterization is the measurement of the Pearson correlation coefficient (Equation 3.36) for the beam generated by the laser and also by SLM with only the diffraction grating being applied to it. The resulting distributions can be seen in Figure 22. This ensures that no statistical bias is added by the setup, and the distributions that will be obtained are due exclusively to the masks applied to the SLM, and not to some intrinsic characteristic of the experimental setup.

Figure 22 – Characterization of the statistic distribution coming from the Pearson correlation coefficient (Equation 3.36) of the experimental setup. Two measurements were made, at the PBS (a) and after the SLM (b) (see Figure 20). For each case, 500 frames were collected.

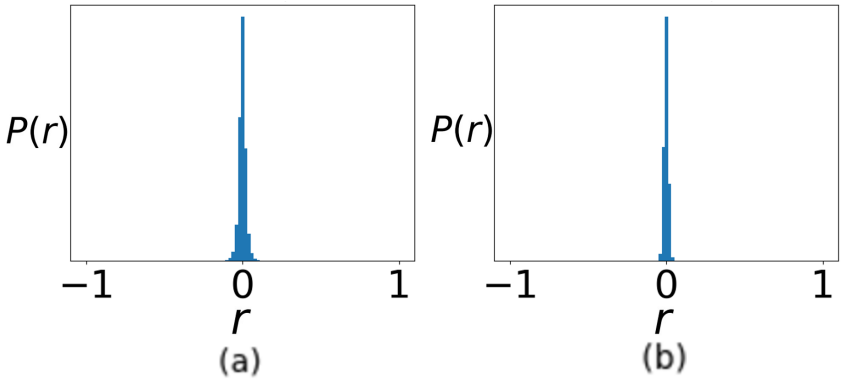

Source: Author (2024)

Figure 22 shows that the beam generated by the laser (a) and that it passes through the SLM (b) after being analyzed by the Pearson correlation coefficient (Equation 3.36) gives approximately a delta distribution. This means that the beam always reproduces itself, in this case, a Gaussian beam.

5.2 EXPERIMENTAL MEASUREMENTS

With the experimental setup fully characterized and calibrated, the thermodynamic beams can be generated and statistically analyzed. The beams are generated with a pseudo-random generator and are symmetric 2D thermodynamic beams as a product of two orthogonal 1D thermodynamic beams with the same width along x and y, $W_x = W_y = W$, and the same energy across the modes, $M_x^2 = M_y^2 = M^2$. This means that the M^2 or available modes are fixed. However, each realization gives an almost random distribution of energy across the modes. It is worth mentioning that different from the usual thermodynamic system, here all microstates ($I_\alpha(\overrightarrow{r})$) can be retrieved at any time. The pseudo-random generator is characterized also by a seed number, that fixes a given ensemble.

For a fixed M^2, there is a specific mode distribution (Equation 2.61). This means that once the M^2 or effective temperature T (Equation 2.60) is fixed, there is a fixed number of modes that the beam can access. Figure 23 shows different beams experimentally generated by the SLM representing the same M^2. In each image, for a given M_x^2, the number of modes is fixed, however, for each realization ($I_\alpha(\overrightarrow{r})$) the energy is distributed differently across the available modes.

Once the beam ensemble is generated, the Pearson correlation coefficient (Equation 3.36) can be used to analyze it, and the statistical distributions in Figure 24 are obtained. Each member of the ensemble, $I_\alpha(x)$, is compared with the ensemble average ,$I(x)$, which gives an $\Delta_\alpha(x)$ (3.34). A given $\Delta_\alpha(x)$ is compared with all the others $\Delta_\alpha(x)$s, each comparison results in a $r_{\alpha\beta}$ and after the all $r_{\alpha\beta}$ pairs are analyzed (Equation 3.36), the distribution is obtained.

In Figure 24, firstly one can observe that there is a characteristic distribution associated with different M^2. For an $M^2 = 1.05$, two peaks can be observed, which shows that the beams in the ensemble are correlated ($r = 1$) or anticorrelated ($r = -1$) with each other. As previously mentioned in Section 3.2, physically this means that the beam wanders, as can be seen in Figure 23 as well.

As the beam temperature or the M^2 increases, the beam loses its spatial coherence and the

Figure 23 – Different beams corresponding to a fixed M^2. The columns have a value of M^2 and six snapshots (rows) of the beam wavefront with this specific M^2. The white dashed line marks the center of measurement. This image corresponds to an experimental realization of Figure 5.

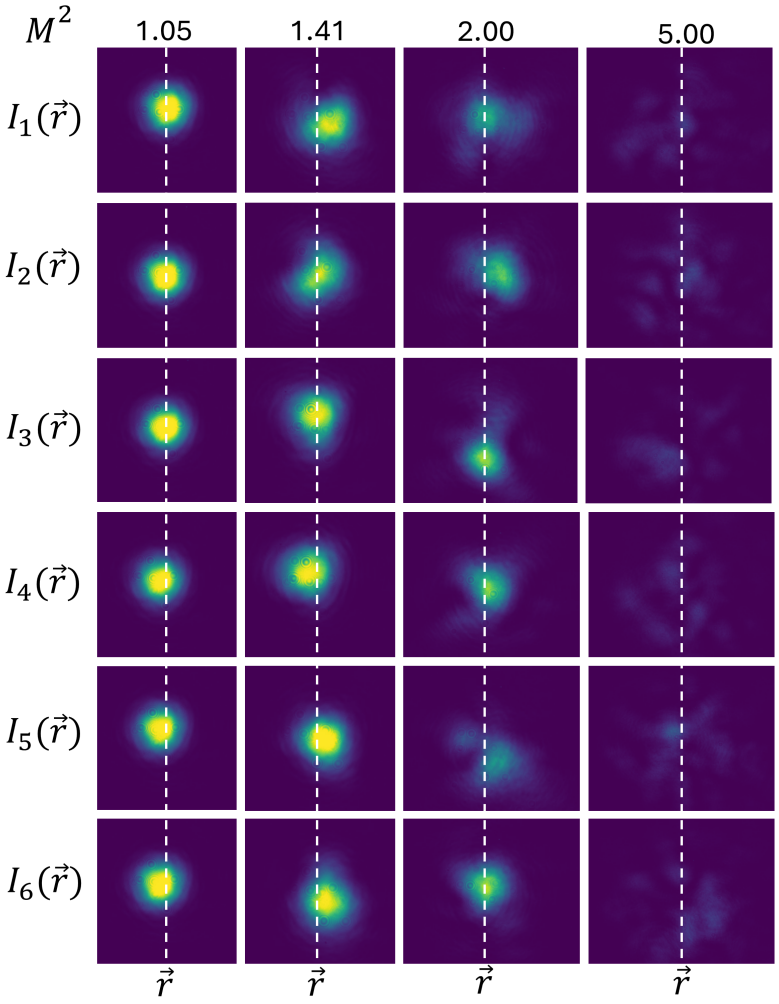

Source: Author (2024)

two peaks collapse into a single peak centered at $r = 0$, and the distribution is Gaussian-like at $M^2 = 5$. As discussed in Section 3.1, the threshold from coherence to partial coherence is a $M^2 = \sqrt{2}$, this can be observed as well in Figure 24, when the distribution start to increase at $r = 0$ and the two peaks at 1 and -1 starts to collapse.

Additionally from the experimental distributions in Figure 24, one can measure the full width at half height for each distribution and compare it with the numerical simulation for the distribution $P(r)$ as a function of both r and M^2, Figure 25.

To further analyze the developed method, the numerical analysis used for Figure 9 was applied to the experimental distribution $P(r)$. The distributions were fitted to obtain the parameter σ. This parameter, experimentally obtained now, was used in Equation 3.40, for

Figure 24 – The masks applied to the SLM (first column) experimentally generate the beams (second column). A beam ensemble (Figure 23) is generated and the Pearson correlation coefficient (Equation 3.36) is analyzed for each ensemble. The third column corresponds to the simulated distribution, obtained from the ideal beams that the mask should generate, and the fourth column shows the experimental distribution. $P(r)$ is normalized and for each distribution, 500 beams were collected to create each ensemble.

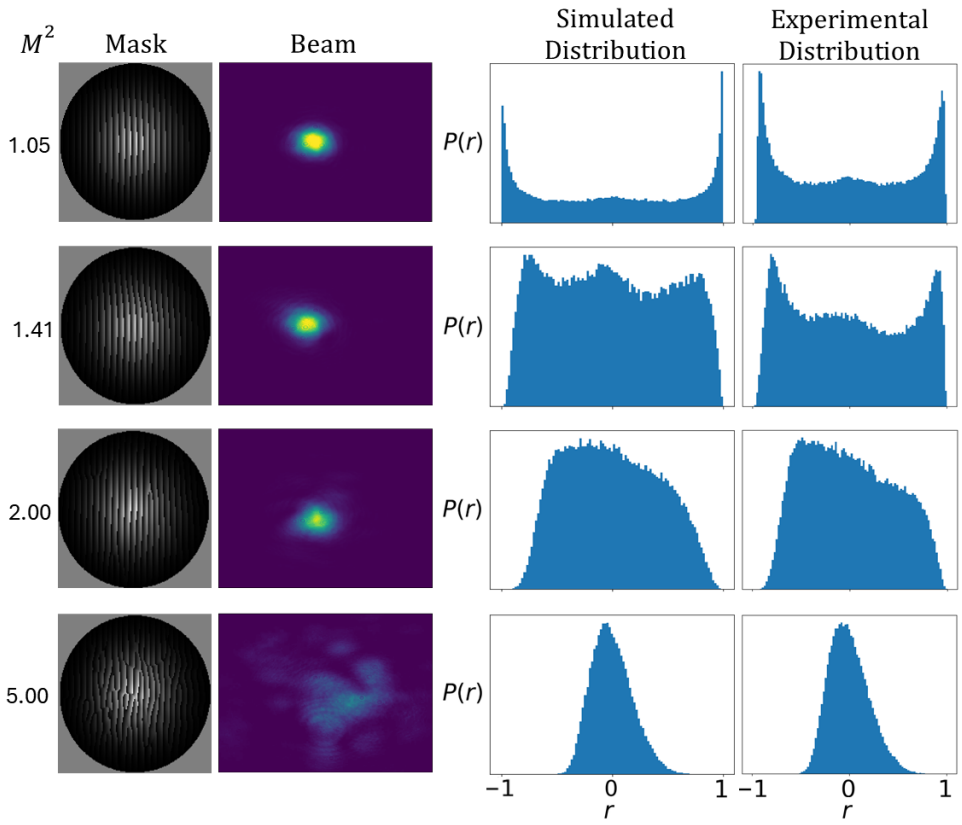

Source: Author (2024)

$f(M^2) = \sigma$. With this, the experimental M^2 was obtained as can be seen in Table 1. The experimental and numerical M^2 coincide well, with less than 10% of difference. The discrepancy can come from imperfections in the experimental setup or a mismatch between Equation 3.39 and the experimental distribution $P(r)$.

Table 1 – Experimental ($M^2_{\text{experimental}}$) and numerical ($M^2_{\text{ensemble}}$) values of M^2. σ is obtained from fitting the experimental distributions $P(r)$ with Equation 3.40.

M^2_{ensemble}	1.05	1.40	2.00	2.50	3.00	4.00	5.00
σ	1.22	0.82	0.53	0.42	0.35	0.25	0.20
$M^2_{\text{experimental}}$	1.04	1.28	1.85	2.28	2.74	3.67	4.58

Source: Author (2024)

Lastly, one more experimental observation is worth mentioning. The statistical analysis obtained from the Pearson correlation coefficient (Equation 3.36) can give insights into how

Figure 25 – Numerical simulation for the distribution $P(r)$ for different M^2. For $M^2 = 1$ or a Gaussian beam, there are two peaks at $r = \pm 1$. As the M^2 increases the two peaks collapse to a single peak centered at $r = 0$. The white dots correspond to the values of r at half-maximum in the experimental distributions.

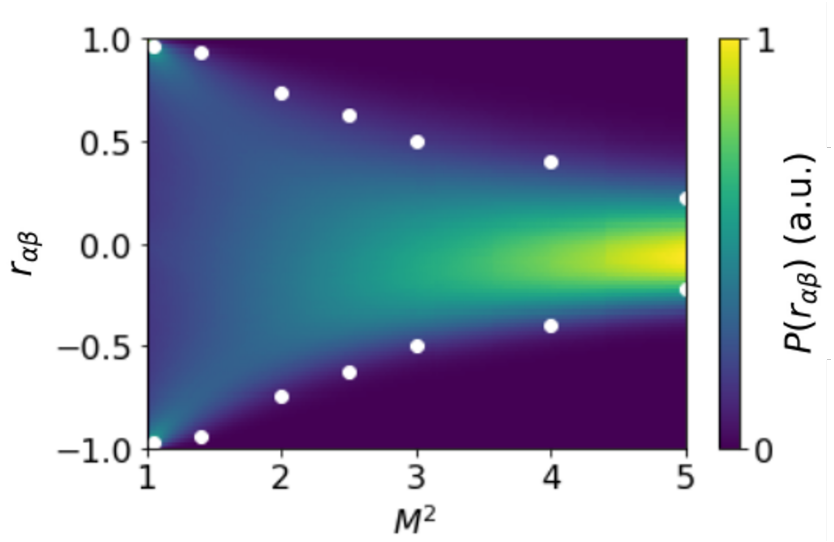

Source: Author (2024)

propagation may affect the beam wavefront.

The same experimental setup as in Figure 20 was used with a free-space Titanium-sapphire laser (800 nm, 40 fs@1 KHz, 1W) for measurements at the PBS and an SLM (pixel size 20 μm; 792x600 resolution) with only a diffraction grating mask the distributions obtained can be seen in Figure 26.

Figure 26 – Characterization of the statistic distribution coming from the Pearson correlation coefficient (Equation 3.36) for a Titanium-sapphire laser. Two measurements were made, at the PBS (a) and the after the SLM (b) (see Figure 20)

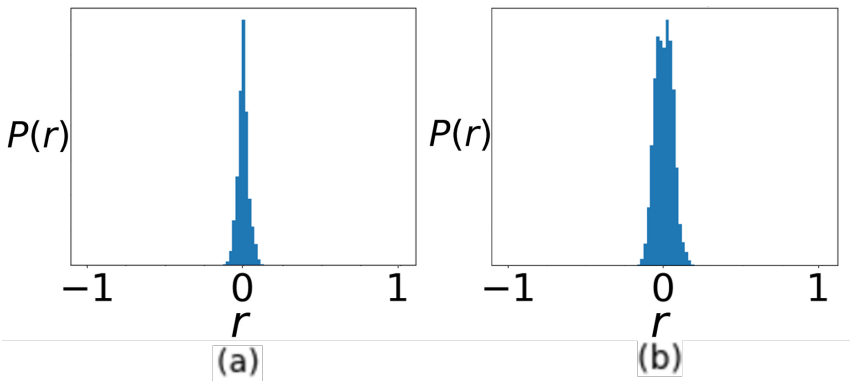

Source: Author (2024)

Figure 26 should be compared with Figure 22. For the mono-mode fiber laser, the propagation does not add significant change to the beam wavefront. However, for the free-space laser,

the propagation affects the beam wavefront. As can be inferred from the broader distribution in (b).

6 CONCLUSION AND PERSPECTIVES

Optical thermodynamics is a promising area of study, and in the last few years has provided powerful new insights into optical systems (Section 2.1). However, it has been used to describe mostly waveguide-based systems. As far as we know, optical thermodynamics concepts were applied only to a few free-space problems, all in the strongly nonlinear regime (PICOZZI et al., 2014). This work extends the current scope application of optical thermodynamics and shows that it can be used to analyze free-space partially coherent light in the linear regime.

Particularly, the use of ladder operators (Section 2.3) is very helpful for the description of free-space system with thermodynamic principles. This, combined with the observation that the thermodynamic beams correspond to the Gaussian Schell-model beams (Section 3.1) allows the use of the thermodynamic description developed here to study partially coherent beams propagating in free-space. Moreover, the proposed thermodynamic description should also be adequate to describe partial coherence in the limit of few modes. This must be particularly useful to study systems with random and/or small imperfections that collectively contribute to changes in the coherence state of light (Section 2.2). An experimental verification of systems that behave as a thermodynamic beam in the few modes regime remains to be found, but laser cavities containing random imperfections seem as candidates to observe such behavior. Another remarkable aspect of the present work is that ordinary tools from statistical optics are inadequate in the few modes regime since the statistics is not Gaussian (C(x,y) is not negligible). However, the statistical analysis of beam ensemble with the Pearson correlation coefficient (Section 3.2) is suited to the few modes regimes. Which analyzes correlations in the beam wavefront and can define the light coherent state in the limit of few available modes. Subsequently, the obtained distributions from the Pearson correlation coefficient can be predicted using statistical arguments (Section 3.3).

Finally, structured light is used to experimentally generate the thermodynamic beams and the proposed statistical analysis is performed over real beam ensembles (Section 5.2). These analyses confirmed the theoretical predictions and matched nicely with the conducted simulations.

Furthermore, the proposed free-space thermodynamic description and subsequently statistical analysis of beams wavefront establishes a new way of studying and measuring coherence in optical systems. Which could be particularly useful for studying light propagating across tur-

bulent and random media. Particularly, the thermodynamic beam could be used to implement channels of communication with different degrees of coherence. Additionally, the statistical analysis here proposed could be used to retrieve information for light propagating in random media, such as biological tissue. Since the random media will produce distortions on the beam wavefront, the statistical analysis could be used to study these distortions and retrieve information regarding the media that the lights propagate in.

REFERENCES

AMARAL, A. M.; JORGE, K. C.; ARAÚJO, C. B. de; MENEZES, L. d. S. Toward single-shot characterization of nonlinear optical refraction, absorption, and scattering of turbid media. *Phys. Rev. A*, v. 102, p. 033503, 2020.

AMBICHL, P.; XIONG, W.; BROMBERG, Y.; REDDING, B.; CAO, H.; ROTTER, S. Super- and anti-principal-modes in multimode waveguides. *Phys. Rev. X*, v. 7, p. 041053, 2017.

ANDREWS, L. C.; PHILLIPS, R. L. *Laser Beam Propagation through Random Media*. Bellingham, Washington: SPIE Press, 2005.

ANDREWS, L. C.; PHILLIPS, R. L.; WEEKS, A. R. Propagation of a gaussian-beam wave through a random phase screen. *Waves in Random Media*, v. 7, n. 2, p. 229–244, 1997.

ARRIZÓN, V.; RUIZ, U.; CARRADA, R.; GONZÁLEZ, L. A. Pixelated phase computer holograms for the accurate encoding of scalar complex fields. *J. Opt. Soc. Am. A*, Optica Publishing Group, v. 24, n. 11, p. 3500–3507, 2007.

BEKSHAEV, A. Y. Intensity moments of a laser beam formed by superposition of hermite-gaussian modes. *ArXiv (Cornell University)*, v. 8, p. 22–25, 2006.

BENTON, S. A.; BOVE, M. *Holographic Imaging*. Hoboken, New Jersey: John Wiley Sons, 2008.

BOLDUC, E.; BENT, N.; SANTAMATO, E.; KARIMI, E.; BOYD, R. W. Exact solution to simultaneous intensity and phase encryption with a single phase-only hologram. *Opt. Lett.*, Optica Publishing Group, v. 38, n. 18, p. 3546–3549, 2013.

CRISPIM, M. J. B.; PEREIRA, C. C. S.; OLIVEIRA, N. T. C.; CHEVROLLIER, M.; OLIVEIRA, R. A. de; MARTINS, W. S.; REYNA, A. S. Intensity correlation scan [ic-scan] technique to characterize the optical nonlinearities of scattering media. *Scientific Reports*, v. 13, n. 1, p. 7239, 2023.

FERRARO, M.; MANGINI, F.; WU, F. O.; ZITELLI, M.; CHRISTODOULIDES, D. N.; WABNITZ, S. Calorimetry of photon gases in nonlinear multimode optical fibers. *Phys. Rev. X*, v. 14, p. 021020, 2024.

GONG, L.; ZHAO, Q.; ZHANG, H.; HU, X.-Y.; HUANG, K.; YANG, J.-M.; LI, Y.-M. Optical orbital-angular-momentum-multiplexed data transmission under high scattering. *Light: Science Applications*, v. 8, n. 1, p. 27, 2019.

HOTELLING, H. New light on the correlation coefficient and its transforms. *Journal of the Royal Statistical Society: Series B (Methodological)*, v. 15, n. 2, p. 193–225, 2018.

HUA, Y.; HU, M.; ZHOU, J.; YINGCHUN, D.; YIN, L. Fast single-shot imaging through scattering media based on a captured speckle pattern without a guidestar. *Applied Physics Letters*, v. 124, n. 14, p. 141101, 2024.

HUISKEN, J.; STAINIER, D. Y. R. Selective plane illumination microscopy techniques in developmental biology. *Development*, v. 136, n. 12, p. 1963–1975, 2009.

ISO Standard 11146-1:2021. *Lasers and laser-related equipment — Test methods for laser beam widths, divergence angles and beam propagation ratios*. [S.l.]: ISO, 2021.

JORGE, K. C.; RIVA, R.; RODRIGUES, N. A. S.; SAKAMOTO, J. ao M. S.; DESTRO, M. G. Scattered light imaging method [slim] for characterization of arbitrary laser beam intensity profiles. *Appl. Opt.*, v. 53, n. 20, p. 4555–4564, 2014.

KOGELNIK, H.; LI, T. Laser beams and resonators. *Applied Optics*, v. 5, n. 10, p. 1550, 1966.

KOROTKOVA, O. *Random Light Beams: Theory and Applications*. Boca Raton, FL: CRC Press, 2014.

LI, R.; CAO, L. Progress in phase calibration for liquid crystal spatial light modulators. *Applied Sciences*, v. 9, n. 10, p. 2012, 2019.

MANDEL, L.; WOLF, E. Spectral coherence and the concept of cross-spectral purity∗. *J. Opt. Soc. Am.*, v. 66, n. 6, p. 529–535, 1976.

MÉLO, L. B. A.; PALACIOS, G. F. R.; CARELLI, P. V.; ACIOLI, L. H.; LEITE, J. R. R.; MIRANDA, M. H. G. de. Deterministic chaos in an ytterbium-doped mode-locked fiber laser. *Opt. Express*, Optica Publishing Group, v. 26, n. 10, p. 13686–13692, 2018.

MILLER, D. A. B. Waves, modes, communications, and optics: a tutorial. *Adv. Opt. Photon.*, Optica Publishing Group, v. 11, n. 3, p. 679–825, 2019.

NAZARATHY, M.; SHAMIR, J. First-order optics—a canonical operator representation: Lossless systems. *Journal of the Optical Society of America*, v. 72, n. 3, p. 356–356, 1982.

NIENHUIS, G. Analogies between optical and quantum mechanical angular momentum. *Philosophical Transactions of the Royal Society A: Mathematical, Physical and Engineering Sciences*, v. 375, n. 2087, p. 20150443, 2017.

NIENHUIS, G.; ALLEN, L. Paraxial wave optics and harmonic oscillators. *Physical Review A*, v. 48, n. 1, p. 656–665, 1993.

OSTROVSKY, A. S. *Coherent-Mode Representations in Optics*. Bellingham, Washington: SPIE Press, 2006.

PAN, M.; FU, Y.; ZHENG, M.; CHEN, H.; ZANG, Y.; DUAN, H.; LI, Q.; QIU, M.; HU, Y. Dielectric metalens for miniaturized imaging systems: progress and challenges. *Adv. Opt. Photon.*, Light: Science Applications, v. 11, n. 1, p. 195, 2022.

PATOUX, A.; AGEZ, G.; GIRARD, C.; PAILLARD, V.; WIECHA, P. R.; LECESTRE, A.; CARCENAC, F.; LARRIEU, G.; ARBOUET, A. Challenges in nanofabrication for efficient optical metasurfaces. *Scientific Reports*, v. 11, n. 1, p. 5620, 2021.

PICOZZI, A. Towards a nonequilibrium thermodynamic description of incoherent nonlinear optics. *Opt. Express*, v. 15, n. 14, p. 9063–9083, 2007.

PICOZZI, A.; GARNIER, J.; HANSSON, T.; SURET, P.; RANDOUX, S.; MILLOT, G.; CHRISTODOULIDES, D. Optical wave turbulence: Towards a unified nonequilibrium thermodynamic formulation of statistical nonlinear optics. *Physics Reports*, v. 542, n. 1, p. 1–132, 2014.

PIERANGELI, D.; TAVANI, A.; MEI, F. D.; AGRANAT, A. J.; CONTI, C.; DELRE, E. Observation of replica symmetry breaking in disordered nonlinear wave propagation. *Nature Communications*, v. 8, n. 1, p. 1501, 2017.

POLETTI, F.; HORAK, P. Description of ultrashort pulse propagation in multimode optical fibers. *Journal of the Optical Society of America B-Optical Physics*, v. 25, n. 10, p. 1645–1645, 2008.

PORRAS, M. A.; ALDA, J.; BERNABEU, E. Complex beam parameter and abcd law for non-gaussian and nonspherical light beams. *Appl. Opt.*, v. 31, n. 30, p. 6389–6402, 1992.

PORRAS, M. A.; ALDA, J.; BERNABEU, E. Nonlinear propagation and transformation of arbitrary laser beams by means of the generalized abcd formalism. *Appl. Opt.*, v. 32, n. 30, p. 5885–5892, 1993.

RAPOSO, E. P.; GONZÁLEZ, I. R. R.; MACÊDO, A. M. S.; LIMA, B. C.; KASHYAP, R.; MENEZES, L. d. S.; GOMES, A. S. L. Evidence of a floquet phase in a photonic system. *Phys. Rev. Lett.*, v. 122, p. 143903, 2019.

ROSALES-GUZMÁN, C.; FORBES, A. *How to Shape Light with Spatial Light Modulators*. Bellingham, Washington: SPIE Press, 2017.

SALEH, B. E. A.; TEICH, M. C. *Fundamentals of Photonics*. Hoboken, NJ: Wiley, 2019.

SHIRAI, T.; DOGARIU, A.; WOLF, E. Mode analysis of spreading of partially coherent beams propagating through atmospheric turbulence. *J. Opt. Soc. Am. A*, v. 20, n. 6, p. 1094–1102, 2003.

SIDORENKO, P.; WU, F. O.; BENDER, N.; WRIGHT, L.; CHRISTODOULIDES, D. N.; WISE, F. Direct observations of thermalization to a rayleigh–jeans distribution in multimode optical fibres. *Nature Physics*, v. 18, p. 685–690, 2022.

SIEGMAN, A. E. Defining, measuring, and optimizing laser beam quality. In: BHOWMIK, A. (Ed.). *Laser Resonators and Coherent Optics: Modeling, Technology, and Applications*. [S.l.]: SPIE, 1993. v. 1868, p. 2 – 12.

STARIKOV, A.; WOLF, E. Coherent-mode representation of gaussian schell-model sources and of their radiation fields. *J. Opt. Soc. Am.*, v. 72, n. 7, p. 923–928, 1982.

SURET, P. Thermodynamic equilibrium of optical waves. *Nature Physics*, v. 18, n. 6, p. 616–617, 2022.

WRIGHT, L. G.; RENNINGER, W. H.; CHRISTODOULIDES, D. N.; WISE, F. W. Nonlinear multimode photonics: nonlinear optics with many degrees of freedom. *Optica*, Optica Publishing Group, v. 9, n. 7, p. 824–841, 2022.

WU, F. O.; HASSAN, A. U.; CHRISTODOULIDES, D. N. Thermodynamic theory of highly multimoded nonlinear optical systems. *Nature Photonics*, v. 13, p. 776–782, 2019.

WU, F. O.; JUNG, P. S.; PARTO, M.; KHAJAVIKHAN, M.; CHRISTODOULIDES, D. N. Entropic thermodynamics of nonlinear photonic chain networks. *Communications Physics*, v. 3, n. 1, p. 216, 2020.

YU, N.; GENEVET, P.; KATS, M. A.; AIETA, F.; TETIENNE, J.-P.; CAPASSO, F.; GABURRO, Z. Light propagation with phase discontinuities: Generalized laws of reflection and refraction. *Science*, v. 334, n. 6054, p. 333–337, 2011.

ZHANG, J.; FAN, J.; MEI, C.; STEINMEYER, G.; HU, M. Bose-einstein condensation of an optical thermodynamic system into a solitonic state. *ArXiv (Cornell University)*, 2024.